

# An Efficient FEniCS Implementation for Coupling Lithium-Ion Battery Charge/Discharge Processes with Fatigue Phase-Field Fracture

Nima Noii<sup>a,1</sup>, Dejan Milijasevic<sup>b</sup>, Amirreza Khodadadian<sup>c,d</sup>, Thomas Wick<sup>b</sup>

<sup>a</sup> Deutsches Institut für Kautschuktechnologie (DIK e.V.)  
Eupener Straße 33, 30519 Hannover, Germany

<sup>b</sup> Institut für Angewandte Mathematik  
Leibniz Universität Hannover, Welfengarten 1, 30167 Hannover, Germany

<sup>c</sup> School of Computer Science and Mathematics  
Keele University, Staffordshire, UK

<sup>d</sup> Research Unit Machine Learning  
Technische Universität Wien, Vienna, Austria

**Published on 5th August 2024**

**Engineering Fracture Mechanics**

<https://doi.org/10.1016/j.engfracmech.2024.110251>

**Volume 306, 1 August 2024, 110251**

---

<sup>1</sup>Corresponding author.

E-mail addresses: nima.noii@dikautschuk.de (N. Noii); dejan.milijasevic@hotmail.de (D. Milijasevic); a.khodadadian@keele.ac.uk (A. Khodadadian); thomas.wick@ifam.uni-hannover.de (T. Wick).

# An Efficient FEniCS Implementation for Coupling Lithium-Ion Battery Charge/Discharge Processes with Fatigue Phase-Field Fracture

Nima Noii<sup>a,2</sup>, Dejan Milijasevic<sup>b</sup>, Amirreza Khodadadian<sup>c,d</sup>, Thomas Wick<sup>b</sup>

<sup>a</sup> Deutsches Institut für Kautschuktechnologie (DIK e.V.)  
Eupener Straße 33, 30519 Hannover, Germany

<sup>b</sup> Institut für Angewandte Mathematik  
Leibniz Universität Hannover, Welfengarten 1, 30167 Hannover, Germany

<sup>c</sup> School of Computer Science and Mathematics  
Keele University, Staffordshire, UK

<sup>d</sup> Research Unit Machine Learning  
Technische Universität Wien, Vienna, Austria

## Abstract

Accurately predicting the fatigue failure of lithium-ion battery electrode particles during charge-discharge cycles is essential for enhancing their structural reliability and lifespan. The fatigue failure of lithium-ion battery electrode particles during charge-discharge cycles poses a significant challenge in maintaining structural reliability and lifespan. To address this critical issue, this study presents a mathematical formulation for fatigue failure in lithium-ion batteries, utilizing the phase-field approach to fracture modeling. This approach, widely employed for fracture failure analysis, offers a comprehensive framework for capturing the complex interplay between mechanical deformation, chemical lithium concentration, and crack formation. Specifically, an additive decomposition of the strain tensor is employed to account for the swelling and shrinkage effects induced by lithium diffusion. Moreover, open-source code (<https://github.com/noiiG>) is provided, constituting a convenient platform for future developments, e.g., multi-field coupled problems. The developed chemo-mechanical model undergoes fatigue failure package is written in FEniCS as a popular free open-source computing platform for solving partial differential equations in which simplifies the implementation of parallel FEM simulations. Several numerical simulations with two different case studies corresponding to monotonic charge process and fatigue charge/discharge process are performed to demonstrate the correctness of our algorithmic developments.

**Keywords:** Lithium-ion batteries, FEniCS, lithiation/delithiation, phase-field fracture, fatigue cracking, multi-physics.

---

<sup>2</sup>Corresponding author.

E-mail addresses: nima.noii@dikautschuk.de (N. Noii); dejan.milijasevic@hotmail.de (D. Milijasevic); a.khodadadian@keele.ac.uk (A. Khodadadian); thomas.wick@ifam.uni-hannover.de (T. Wick).

## 1. Introduction

In pursuit of the Climate Protection Law and the overarching goal of achieving net-zero greenhouse gas emissions by 2050, the European Union (EU) recognizes the pivotal role of cleaner and renewable energy sources, complemented by innovative technologies [1, 2]. Within the industrial landscape, the adoption of lithium-ion batteries emerges as a key player in facilitating this transition. Lithium-ion batteries, renowned for their energy density and versatility, serve as a cornerstone for storing renewable energy and powering electric vehicles, thus reducing reliance on traditional fossil fuels [3, 4]. The integration of lithium-ion battery technology in industrial applications not only aligns with the EU's climate ambitions but also contributes to creating a sustainable energy infrastructure [5, 6]. By embracing these advanced energy storage solutions, the EU strives not only to meet its climate targets but also to drive a paradigm shift towards a more environmentally conscious and technologically advanced industrial sector.

These batteries find major applications in various systems, including portable electronic devices like smartphones, laptops, and tablets, where compact and efficient power sources are imperative. Additionally, they play a crucial role in powering electric vehicles, contributing to sustainable and environmentally friendly transportation [7]. Moreover, lithium-ion batteries are integral to renewable energy systems, storing harvested energy from sources such as solar panels for future use [8]. Their versatility extends to medical devices, aerospace technology, and various other fields with high demands for reliable and efficient power solutions [9].

Within the lithium-ion battery charging relies on a critical process through the migration of positively charged lithium ions ( $\text{Li}^+$ ) from the anode to the cathode [10, 11]. The anode, typically composed of materials like graphite, lithium titanate ( $\text{Li}_4\text{Ti}_5\text{O}_{12}$ ), or metal oxides such as  $\text{SnO}_2$  or  $\text{Fe}_3\text{O}_4$ , acts as a host for  $\text{Li}^+$  ions. These ions traverse the electrolyte, usually a lithium salt dissolved in a solvent like ethylene carbonate and dimethyl carbonate, facilitating ion transport. Diffusion through the electrolyte occurs due to a concentration gradient, influenced by factors like temperature and electrolyte type.  $\text{Li}^+$  ions then pass through a separator material, like ceramic-coated separators or polyethylene (PE), under the electric field created by the anode-cathode voltage difference, preventing short circuits. Finally, at the cathode, materials such as lithium cobalt oxide ( $\text{LiCoO}_2$ ) or lithium iron phosphate ( $\text{LiFePO}_4$ ) facilitate the acceptance of  $\text{Li}^+$  ions and the conversion of electrical energy into chemical energy for storage. During the discharging phase, the process undergoes a reversal.

The challenges posed by degradation mechanisms induced during the lithiation process are particularly pronounced in lithium-ion batteries, especially those featuring high-capacity electrodes like silicon (Si). These degradation mechanisms, highlighted in studies such as [12], possess the potential to limit the overall lifespan of the batteries. A pivotal factor contributing to the degradation mechanisms in electrochemical systems is the damage sustained within electrode particles, as highlighted in [13]. This damage results from the stresses generated by the uneven expansion and contraction of electrode materials during the insertion and extraction of lithium ions, as discussed in [14]. Therefore, high stress concentration results in the fractures within electrode particles, which significantly impact battery performance and efficiency.

Primarily, the breakage disrupts electronic connectivity between particles, leading to

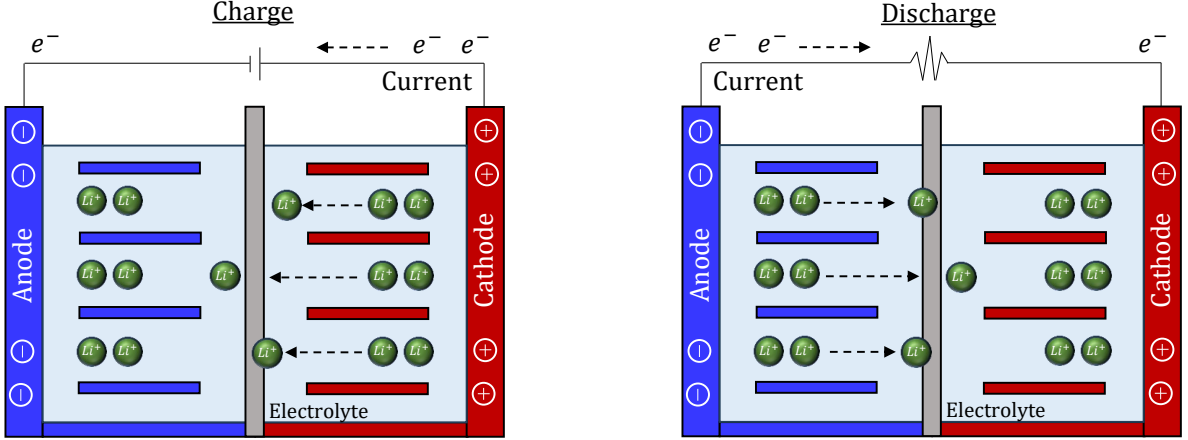


**Figure 1:** During the charging process, lithium ions (green circles) migrate from the positive electrode (red) to the negative electrode (blue) through the electrolyte (light blue), driven by an external electrical potential. Simultaneously, electrons flow from the positive electrode to the negative electrode, completing the circuit. Once all the ions have transferred, the battery is fully charged and ready to power devices. During discharging, the reverse process occurs.

a reduction in the effective amount of active material available within a cell. This directly influences the overall capacity and efficiency of the battery. Additionally, the fractures expose fresh surfaces on the electrode particles, serving as sites for additional parasitic side reactions, a phenomenon well-documented in [15]. One specific manifestation of this phenomenon is the formation and growth of the solid electrolyte interphase (SEI). The SEI is a layer that forms on the electrode surface and can detrimentally affect battery performance, as explained in [16]. Consequently, the available amount of lithium within the system diminishes over time due to these additional reactions, further impacting the battery's overall efficiency and longevity.

A significant degradation mechanism, known as *fatigue cracking*, arises in lithium-ion battery electrode particles, manifesting as the development of cracks within the electrode material over repeated charging and discharging cycles, as discussed in [17, 18]. This phenomenon is particularly prevalent in high-capacity electrode materials like silicon, presenting a substantial challenge to the overall performance and lifespan of lithium-ion batteries. This cyclic expansion and contraction impose mechanical stress and strain on the electrode particles, a phenomenon elucidated in [19]. Over time, the accumulated stress can exceed the material's structural tolerance, initiating and propagating microscopic cracks, termed fatigue cracks, as detailed in [18]. These cracks compromise the structural integrity of the electrode particles, resulting in a decline in the overall capacity and efficiency of the battery. Firstly, these cracks establish pathways for the electrolyte to infiltrate deeper into the electrode material, heightening the likelihood of undesirable side reactions and detrimentally affecting the overall electrochemical performance of the battery. Secondly, the fractured particles may detach from the electrode, resulting in a loss of active material and a subsequent reduction in the overall capacity of the battery. Therefore, the present study devoted into the fatigue failure theory in lithium-ion battery electrode particles.

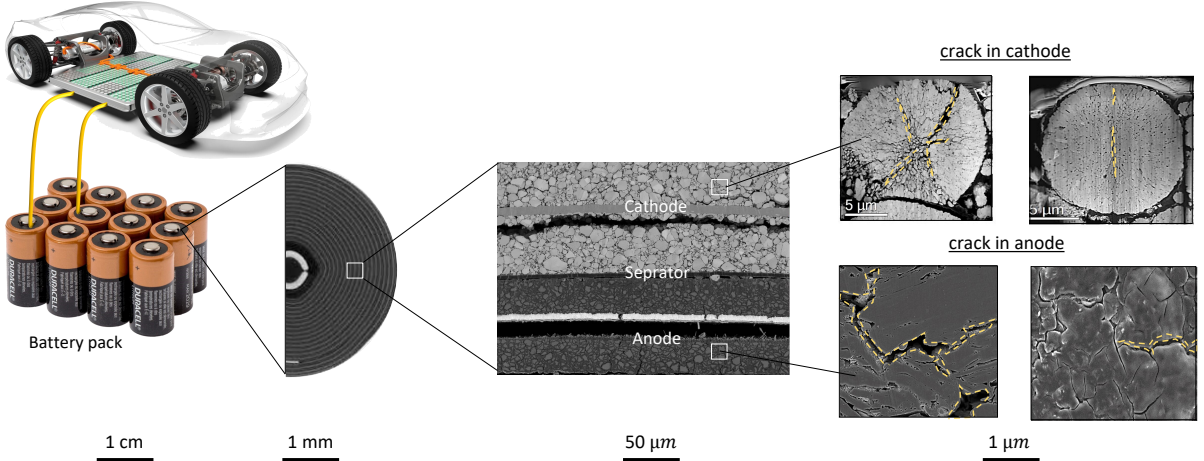


**Figure 2:** The reprocessing of lithium-ion batteries in the EV industry using direct battery packs (reprinted from [20]). X-ray tomography of lithium-ion batteries including its cross section showing the internal structure of a lithium-ion battery. By zoom-in into the rolling cross-section structure of the battery, three major counterparts including the cathode, separator and anode are depicted. This has been captured through scanning electron microscopy (SEM) [21]. Magnified virtual slice to shows cracking and delamination induced lithium diffusion in both SEM cross-sections of the cracking cathode electrode [22] and a graphite electrode which exhibits cracks on the anode electrode reported from [23].

In the literature, there are various ways to study how lithium-ion batteries degrade during the lithiation or delithiation process. Xu et al. [12] investigated a cohesive zone models for the lithiation process of electrodes, where the crack path was decided beforehand. Ryu et al. [24] took a different route. They used a linear fracture mechanics approach to check out how silicon nanowires (Si-NWs) break down during the lithiation/delithiation processes. Their study looked at big changes happening during lithiation, considering how pressure differences affect the spread of lithium. Then, Zhu et al. [25] used an extended finite element method approach to track crack propagation in primary particles. They further study how the stress due to the lithiation results in the cracks in  $\text{Li}^+$  ion electrode particles.

The variational approach to fracture by Francfort and Marigo and the related regularized formulation [26], which is also commonly referred to as a phase-field model of fracture, e.g., the review studies [27, 28, 29, 30, 31], is a widely accepted framework for modeling and computing the fracture failure phenomena in elastic solids. Thus, since the computational modeling of such complex behavior for fatigue cracking for lithium-Ion battery electrode particles is required, in this study the phase-field method of failure is used. The origin of the phase-field method is the variational formulation of Griffith's fracture [32] and its following regularization [33], in which the crack propagation is coupled with a critical value of the energy release rate. Based on this, many modifications have been developed for special applications. The wide variety of phase-field fractures include for example thermal shocks and thermo-elastic-plastic solids [34, 35, 36], pressurized fractures [36, 37, 38, 39, 40, 41], proppant-filled fractures [42], fluid-filled fractures [43, 44, 45, 46, 47, 48, 49], dynamic fracture [50, 51, 52, 53], ductile fracture [54, 55, 56, 57], cohesive fracture [58, 59, 60], fractures in functionally graded materials and composites [61, 62], fracture resistance with topology optimization [63, 64, 65], and material identifi-

cation for fracture [66, 67].

While extensive research has been conducted on degradation mechanisms associated with lithium diffusion-induced fracture, fatigue cracking has received relatively less attention. Even though understanding fatigue failure in lithium-ion battery electrode particles is crucial for explaining how cracks nucleate and propagate within the electrode materials, developing a rigorous mathematical model for this phenomenon remains a challenge.

In this manuscript to address this issue, we aim to formulate a mathematical framework to capture the complex interplay between chemical lithium concentration, crack formation, and mechanical deformation within the electrode material. Therefore, the coupling of chemical lithium concentration to the crack phase-field is achieved through a constitutive work density function. This function effectively captures the degradation in stored elastic energy due to the accumulation of damage and the dissipated energy associated with lithium concentration and crack formation. By incorporating the coupling between mechanical deformation, chemical lithium concentration, and crack formation, the formulation can accurately predict the degradation of electrode materials under repeated charging and discharging cycles. This understanding is crucial for enhancing battery performance and the lifespan in various electronic applications.

Another important contribution of this paper is the accompanying open-source programming codes published on GitHub<sup>3</sup>. Since, we strongly believe and agree with the reasons for open-source research software initiatives outlined in [68, 69], that is, codes must be available at some point. Recently, different codes for a variety of boundary value problems regarding phase-field modeling of fracture in the different platforms have been reported. These include available codes, [70, 71, 72] in FEniCS [73, 74, 75, 76, 77] in ABAQUS, [78] in C++ (Specifically, in DEAL.II), [79, 80] in COMSOL, [81] in JULIA. Recently, Noii et al. [66] provided compact open-source codes for phase-field fracture for brittle materials, ductile materials (gradient-extended plasticity), thermoelasticity, and fatigue fracture in MATLAB. Since we believe that it is vital to implement our implementation within open-source code that can be used and developed with other researchers easily, we have used FEniCS in this manuscript. Thus, this manuscript besides the current work [18] recasts some aspects of the phase-field formulation with different fatigue degradation formulations toward enabling a highly efficient open-source FEniCS implementation for this complex problem. To summarize, this work has focused on these key points:

- To develop a fatigue failure formulation of lithium-ion battery electrode particles during charge/discharge cycles;
- To provide an efficient open-source FEniCS implementation that is devoted to chemo-mechanical model undergoing fatigue failure in lithium-ion battery;
- To provide high-performance computing through solving the multi-field equations through multifrontal massively parallel sparse (MUMPS) and built-in support for MPI running;
- Two- and three-dimensional boundary value problems are investigated to observe the influence of the randomly distributed micro cavities in electrode particles.

---

<sup>3</sup>The compact open-source code that can be used to reproduce the examples is available online at <https://github.com/noiiG>.

The paper is structured as follows. In Section 2, a mathematical formulation for fatigue cracking in lithium-ion battery electrode particles is presented. The degradation processes are modeled using phase-field fracture mechanics, leading to a comprehensive algorithmic framework. In Appendix, we have provided an efficient open-source FEniCS implementation that is devoted to chemo-mechanical model undergoes fatigue failure in lithium-ion battery is discussed in detail. Section 3 validates the formulation and implementation through four numerical simulations including diverse case studies, delivering the methodology's accuracy and versatility. These include both two- and three-dimensional settings. Finally, the concluding section provides the key achievements, highlights the development of a robust mathematical formulation and algorithmic framework, and proposes ideas for future exploration.

## 2. Phase-field modeling of fracture in lithium-ion battery electrode particles

In this section, we provide fatigue failure theory for chemo-elasticity media induced fracturing response. This includes the coupling of the deformation field, lithium diffusion, and phase-field fracture model to describe fatigue damage mechanisms. Here, the phase-field framework is aimed for regularizing sharp interfaces, consisting of incorporating a continuous field variable – the so-called order parameter – denoted by  $d$  which differentiates between physical phases within a given system through a smooth transition. The coupling of elasticity to the crack phase-field is achieved by a constitutive work density function, which is characterized by a degraded stored elastic energy and the accumulated dissipated energy due to the damage.

Three governing equations corresponding to our multi-field problems are employed to characterize the constitutive formulations for the mechanical deformation, lithium chemical potential, as well as the fracture phase-field. Finally, we describe strong and variational formulations of the coupled multi-physics problem.

### 2.1. Primary fields for the multi-field problem

Let  $\mathcal{B} \subset \mathbb{R}^\delta$  be an arbitrary solid domain,  $\delta = \{2, 3\}$  with a smooth boundary  $\partial\mathcal{B}$  (Figure 3). We assume Dirichlet boundary conditions on  $\partial_D\mathcal{B}$  and Neumann boundary conditions on  $\partial_N\mathcal{B} := \Gamma_N \cup \mathcal{C}$ , where  $\Gamma_N$  denotes the outer domain boundary and  $\mathcal{C} \in \mathbb{R}^{\delta-1}$  is the crack boundary, as illustrated in Figure 3(b). The response of the fracturing solid at material points  $\mathbf{x} \in \mathcal{B}$  and time  $t \in \mathcal{T} = [0, T]$  is described by the displacement field  $\mathbf{u}(\mathbf{x}, t)$  and the crack phase-field  $d(\mathbf{x}, t)$  as

$$\mathbf{u} : \begin{cases} \mathcal{B} \times \mathcal{T} \rightarrow \mathbb{R}^\delta \\ (\mathbf{x}, t) \mapsto \mathbf{u}(\mathbf{x}, t) \end{cases} \quad \text{and} \quad d : \begin{cases} \mathcal{B} \times \mathcal{T} \rightarrow [0, 1] \\ (\mathbf{x}, t) \mapsto d(\mathbf{x}, t) \end{cases}. \quad (1)$$

Intact and fully fractured states of the material are characterized by  $d(\mathbf{x}, t) = 0$  and  $d(\mathbf{x}, t) = 1$ , respectively. In order to derive the variational formulation, the following space is first defined. For a domain with sufficiently small domain  $A \subset \mathbb{R}^\delta$ , we set

$$\mathbf{H}^1(\mathcal{B}, A) := \{v : \mathcal{B} \times \mathcal{T} \rightarrow A : dv \in \mathbf{H}^1(A)\}. \quad (2)$$

We also denote the vector valued space  $\mathbf{H}^1(\mathcal{B}, A) := [\mathbf{H}^1(\mathcal{B}, A)]^\delta$  and define

$$\mathcal{W}_{\bar{\mathbf{u}}}^{\mathbf{u}} := \{\mathbf{u} \in \mathbf{H}^1(\mathcal{B}, \mathbb{R}^\delta) : \mathbf{u} = \bar{\mathbf{u}} \text{ on } \partial_D^{\mathbf{u}}\mathcal{B}\}. \quad (3)$$

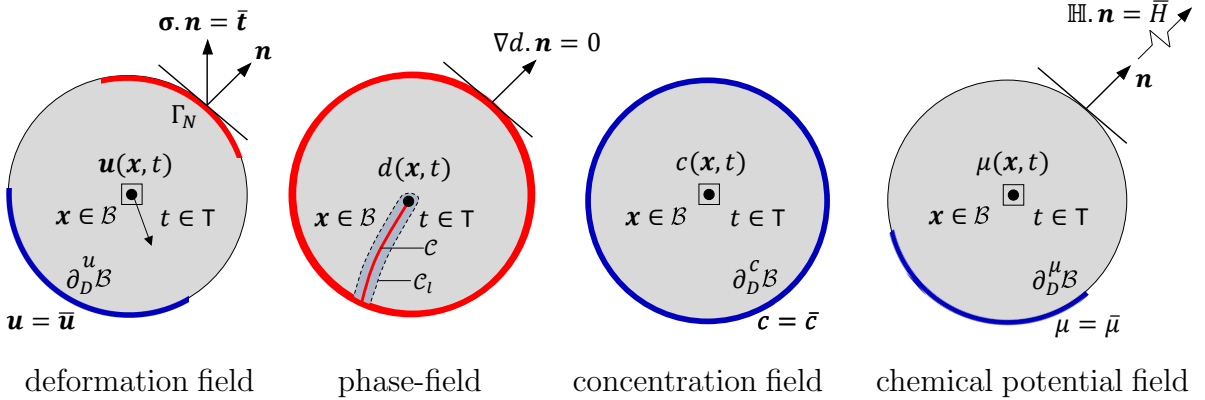


**Figure 3:** Notations for coupling chemo-elasticity with phase-field fatigue fracture. The deformation field  $\mathbf{u}$ , phase-field  $d$ , and lithium-ion concentration  $c$ , and chemical potential field  $\mu$  are defined on the solid domain  $\mathcal{B}$ .

Concerning the crack phase-field, we set

$$\mathcal{W}^d := H^1(\mathcal{B}) \quad \text{and} \quad \mathcal{W}_{d_n}^d := \{d \in H^1(\mathcal{B}, [0, 1]) : d \geq d_n\}, \quad (4)$$

where  $d_n$  is the damage value at a previous time instant. Note that  $\mathcal{W}_{d_n}^d$  is a non-empty, closed and convex subset of  $\mathcal{W}^d$ , and introduces the evolutionary character of the phase-field, incorporating an irreversibility condition in incremental form. Additionally, to formulate chemo-mechanical model undergoes fatigue failure, we require to define lithium concentration field  $c(\mathbf{x}, t)$  and lithium chemical potential field  $\mu(\mathbf{x}, t)$  as:

$$c : \begin{cases} \mathcal{B} \times \mathcal{T} \rightarrow \mathcal{R} \\ (\mathbf{x}, t) \mapsto c(\mathbf{x}, t) \end{cases} \quad \text{and} \quad \mu : \begin{cases} \mathcal{B} \times \mathcal{T} \rightarrow \mathcal{R} \\ (\mathbf{x}, t) \mapsto \mu(\mathbf{x}, t) \end{cases}. \quad (5)$$

The lithium chemical potential field is defined in the following space:

$$\mathcal{W}_\bar{\mu}^\mu := \{H^1(\mathcal{B}) : \mu = \bar{\mu} \text{ on } \partial_D^\mu \mathcal{B}\}, \quad (6)$$

and for the variation of lithium concentration mass content (or also named as the relative change of lithium concentration content), we consider the following space:

$$\mathcal{W}^c := \{H^1(\mathcal{B}) : c = \bar{c} \text{ on } \partial_D^c \mathcal{B}\}. \quad (7)$$

The gradient of the displacement field defines the symmetric strain tensor of the geometrically linear theory as

$$\boldsymbol{\varepsilon} = \nabla_s \mathbf{u} = \text{sym}[\nabla \mathbf{u}] := \frac{1}{2} [\nabla \mathbf{u} + \nabla \mathbf{u}^T]. \quad (8)$$

In view of the small strain hypothesis, the total strain tensor is additively decomposed into an elastic part  $\boldsymbol{\varepsilon}^e$  and a chemical strain due to the local lithium concentration part  $\boldsymbol{\varepsilon}^c$  as

$$\boldsymbol{\varepsilon}(\mathbf{u}; \mathbf{x}) = \boldsymbol{\varepsilon}^e(\mathbf{u}, c; \mathbf{x}) + \boldsymbol{\varepsilon}^c(c; \mathbf{x}). \quad (9)$$

Typically, the chemical strain is considered as a hydrostatic dilatation, and is defined by:

$$\boldsymbol{\varepsilon}^c(c; \mathbf{x}) := \frac{\Omega_c(c - c_0)}{3} \mathbf{I}. \quad (10)$$

Here,  $\Omega_c$  refers to the lithium partial molar volume, and the term  $c - c_0$  results from the consideration of the substitutional nature of lithium-ion diffusion. Here,  $c_0$  describes the reference lithium concentration in the stress-free state which is set as zero in this study.

The solid  $\mathcal{B}$  is loaded by prescribed deformations and external tractions on the boundary, defined by time-dependent Dirichlet conditions and Neumann conditions

$$\mathbf{u} = \bar{\mathbf{u}}(\mathbf{x}, t) \text{ on } \partial_D^u \mathcal{B} \quad \text{and} \quad \boldsymbol{\sigma} \cdot \mathbf{n} = \bar{\boldsymbol{\tau}}(\mathbf{x}, t) \text{ on } \partial_N^u \mathcal{B}, \quad (\text{BC.E})$$

where  $\mathbf{n}$  is the outward unit normal vector on the surface  $\partial \mathcal{B}$ . The stress tensor  $\boldsymbol{\sigma}$  is the thermodynamic dual to  $\boldsymbol{\varepsilon}$  and  $\bar{\boldsymbol{\tau}}$  is the prescribed traction vector.

Prescribed Dirichlet boundary condition and Neumann boundary condition for the lithium chemical potential can be described by:

$$\mu = \bar{\mu}(\mathbf{x}, t) \text{ on } \partial_D^\mu \mathcal{B} \quad \text{and} \quad \mathbb{H} \cdot \mathbf{n} = \bar{H}(\mathbf{x}, t) \text{ on } \partial_N^\mu \mathcal{B}, \quad (\text{BC.F})$$

through the lithium flux vector  $\mathbb{H}$ , the imposed lithium chemical potential  $\bar{\mu}$  on the boundary surface, lithium transport  $\bar{H}$  on the Neumann boundary surface. The fracture in chemomechanical process is due to stress concentration of the chemical load through a concentration field of  $\text{Li}^+$  or  $\text{Li}^+$  flux.

## 2.2. Constitutive energy density functions for chemo-elasticity

In the following formulation, we define the constitutive energy density functions for the elastic energy density  $W_{\text{elas}}$ , and lithium-ion contribution  $W_{\text{Li-ion}}$  to establish the multi-field evolution problem in terms of the primary fields.

**2.2.1. Elastic contribution.** The elastic energy density  $W_{\text{elas}}$  is expressed in terms of the effective strain energy density  $\psi_e(\boldsymbol{\varepsilon}^e)$ . In our formulation, in order to prevent fracture in compression, a decomposition of the effective strain energy density into *fractured* and *unfractured* parts is employed. As we already mentioned, a major contribution for the damage mechanisms of the lithium-ion battery electrode particles is swelling and shrinkage effects [14]. Thus, we perform an additive decomposition of the strain tensor into *volume-changing* (volumetric) and *volume-preserving* (deviatoric) counterparts

$$\boldsymbol{\varepsilon}^e(\mathbf{u}, \mathbf{x}) = \boldsymbol{\varepsilon}^{e,\text{vol}}(\mathbf{u}, \mathbf{x}) + \boldsymbol{\varepsilon}^{e,\text{dev}}(\mathbf{u}, \mathbf{x}),$$

where

$$\begin{aligned} \boldsymbol{\varepsilon}^{e,\text{vol}}(\mathbf{u}, \mathbf{x}) &:= \mathbb{P}^{\text{vol}} : \boldsymbol{\varepsilon}^e, \quad \text{with} \quad \mathbb{P}_{ijkl}^{\text{vol}} := \frac{1}{3} \delta_{ij} \delta_{kl}, \\ \boldsymbol{\varepsilon}^{e,\text{dev}}(\mathbf{u}, \mathbf{x}) &:= \mathbb{P}^{\text{dev}} : \boldsymbol{\varepsilon}^e, \quad \text{with} \quad \mathbb{P}^{\text{dev}} := \mathbb{I} - \frac{1}{3} \mathbf{I} \otimes \mathbf{I} \quad \text{and} \quad \mathbb{I}_{ijkl} := \frac{1}{2} (\delta_{ik} \delta_{jl} + \delta_{il} \delta_{jk}), \end{aligned} \quad (11)$$

with the first and second invariants of the elastic strain denoted as  $I_1(\boldsymbol{\varepsilon}^e) := \text{tr}[\boldsymbol{\varepsilon}^e]$  and  $I_2(\boldsymbol{\varepsilon}^e) := \text{tr}[(\boldsymbol{\varepsilon}^e)^2]$ . The effective strain energy function  $\psi_e(\boldsymbol{\varepsilon}^e)$  is additively decomposed into fractured and unfractured contributions:

$$\psi_e(I_1(\boldsymbol{\varepsilon}^e), I_2(\boldsymbol{\varepsilon}^e)(\mathbf{x})) = \psi_e^+(I_1, I_2) + \psi_e^-(I_1), \quad (12)$$

such that

$$\psi_e^+ = H^+[I_1]\psi_e^{vol}(I_1) + \psi_e^{dev}(I_1, I_2) \quad \text{and} \quad \psi_e^- = (1 - H^+[I_1])\psi_e^{vol}(I_1). \quad (13)$$

Therein,  $H^+[I_1(\boldsymbol{\varepsilon}^e)]$  is a *positive Heaviside function* which returns one and zero for  $I_1(\boldsymbol{\varepsilon}^e) > 0$  and  $I_1(\boldsymbol{\varepsilon}^e) \leq 0$ , respectively. We note that in this paper the volumetric and deviatoric counterparts of the energy take the following forms:

$$\psi_e^{vol}(I_1) = \frac{K}{2}I_1^2 = \frac{K}{2}\left(\boldsymbol{\varepsilon}^{e,vol} : \mathbf{I}\right)^2 \quad \text{and} \quad \psi_e^{dev}(I_1, I_2) = \mu\left(\frac{I_1^2}{3} - I_2\right) = \mu\boldsymbol{\varepsilon}^{e,dev} : \boldsymbol{\varepsilon}^{e,dev}. \quad (14)$$

Here,  $K = \lambda + \frac{2}{3}\mu > 0$  is the bulk modulus which includes the elastic Lamé's first constant denoted by  $\lambda$  and the shear modulus  $\mu$ . The total elastic contribution to the pseudo-energy (27) finally reads

$$W_{elas}(\boldsymbol{\varepsilon}^e, d; \alpha) := g(d) [\psi_e^+(I_1, I_2)] + \psi_e^-(I_1, I_2), \quad (15)$$

where  $g(d)$  is the *elastic degradation function*, which takes in a simple quadratic form as:

$$g(d) = (1 - \kappa_d)(1 - d)^2 + \kappa_d. \quad (16)$$

Following [82, 83], the small residual scalar  $0 < \kappa_d \ll 1$  is used to prevent numerical instabilities. The global mechanical form as a *first* PDE formulated for the equilibrium equation of the solid body which can be represented through first-order PDE for the multi-field system as

$$\operatorname{Div} \boldsymbol{\sigma}(\mathbf{u}, c, d) + \bar{\mathbf{b}} = \mathbf{0}, \quad (\text{E})$$

such that dynamic motion is neglected (i.e., quasi-static response), and we denote  $\bar{\mathbf{b}}$  as a prescribed body force.

**2.2.2. Lithium-ion contribution.** To formulate the constitutive equation for the chemo-elasticity, this follows by the mass conservation for the lithium concentration which includes chemical concentration and a solid matrix within the bulk material. The lithium flux vector given in (BC.F) can be described through the negative direction of the material gradient of the lithium chemical potential  $\nabla\mu$  through the diffusivity, based on the linear Onsager relationship (similar to Fick's first law and Fourier's law of heat conduction) [84]:

$$\mathbb{H} := -\mathbf{K}(c, d) \nabla\mu = \mathbf{K} \cdot \mathbb{B} \quad \text{with} \quad \mathbb{B} = -\nabla\mu \quad \text{in } \mathcal{B}. \quad (17)$$

Therefore, Lithium-ions move from areas of high chemical potential to regions with lower chemical potential. In (17), the concentration diffusivity tensor is given by isotropic tensor  $\mathbf{K}$  which is described based on the lithium concentration,  $c$  as well as the crack phase-field  $d$ , as follows:

$$\mathbf{K}(c, d) = g(d) \frac{D}{R\vartheta} c \mathbf{I}. \quad (18)$$

Here,  $D$  denotes the the lithium diffusion coefficient,  $R$  indicates universal gas constant that is  $8.314 \text{ J} \cdot \text{K}^{-1} \cdot \text{mol}^{-1}$ , and  $\vartheta$  represents the ambient temperature (see [18, 85]).

Therefore, the conservation of the lithium ion mass which reflects the *second* PDE within within chemo-mechanical fracturing setting reads

$$\dot{c} - \bar{r}_L + \text{Div}[\mathbb{H}] = 0, \quad (\text{C})$$

by a given/imposed chemical source  $\bar{r}_L$  per unit volume of the initial setting  $\mathcal{B}$  describing the chemical source transporting process in the lithium ion battery. Here,  $\mathbb{H}$  is the (17) lithium-ion flux vector, see Section 2.3.2.

Following [86], the lithium-ion density function takes the following form

$$W_{Li-ion}(c) = \mu_0 c + R\vartheta N_L \left( \Theta_L \ln \Theta_L + (1 - \Theta_L) \ln (1 - \Theta_L) \right), \quad (19)$$

here,  $\mu_0$  is the reference chemical potential and  $\ln$  denotes the natural logarithm. For other two parameters, i.e.,  $N_L$ , and  $\Theta_L$  are used in  $W_{Li-ion}(c)$ , we have:

- **Number of moles of lattice sites of lithium network  $N_L$ .** The number of moles of lattice sites in the lithium metal network is denoted as  $N_L$  where constant interstitial sites concentration is assumed  $\nabla N_L = 0$ .
- **Occupancy fraction of lithium network  $\Theta_L$ .** Let low occupancy of interstitial of lithium network, thus we have  $\Theta_L = c/N_L$  for  $0 < \Theta_L \ll 1$ .
- **Isothermal condition  $\vartheta$ .** Here, we assured that isothermal conditions for thermal effect, such that  $\dot{\vartheta} = 0$  and  $\nabla \vartheta = 0$ .

We note that this phenomenological approach for degradation mechanism of lithium-ion battery has some similarity to the diffusion of hydrogen and oxygen in fractured metals, where the solute becomes entrapped ahead of the crack tip [86, 87].

**2.2.3. Fracture contribution.** The phase-field contribution is expressed in terms of the crack surface energy density  $\gamma_l$  and the fracture length-scale parameter  $l_d$  that governs the regularization. In particular, the sharp-crack surface topology  $\mathcal{C}$  is regularized by a functional  $\mathcal{C}_{l_d}$ , as outlined in [88] and [36, 89, 90]. This geometrical perspective is in agreement with the framework of [33], which was conceived as a  $\Gamma$ -convergence regularization of the variational approach to Griffith fracture [32]. For the case of isotropic materials, the regularized functional reads

$$\mathcal{C}_{l_d}(d) = \int_{\mathcal{B}} \gamma(d, \nabla d; l_d) dV. \quad (20)$$

In line with standard phase-field models, an isotropic surface density function  $\gamma$  is defined as

$$\gamma(d, \nabla d) := \frac{1}{c_d} \left( \frac{\omega(d)}{l_d} + l_d \nabla d \cdot \nabla d \right) \quad \text{with} \quad c_d := 4 \int_0^1 \sqrt{\omega(b)} db, \quad (21)$$

where  $\omega(d)$  is a monotonic and continuous *local fracture energy function* such that  $\omega(0) = 0$  and  $\omega(1) = 1$ . A variety of suitable choices for  $\omega(d)$  are available in the literature [91, 92,

93]. Here, the widely adopted linear and quadratic formulations are considered, which yield, respectively, models with and without an elastic stage. Specifically, we define

$$\omega(d) := \begin{cases} d & \Rightarrow c_d = 8/3 \\ d^2 & \Rightarrow c_d = 2 \end{cases} \quad \begin{array}{l} \text{model with an elastic stage,} \\ \text{model without an elastic stage.} \end{array} \quad (22)$$

Therefore, we can derive  $d$  (the crack phase-field) by minimizing diffusive crack surface  $\mathcal{C}_l(d)$ , as follows

$$d = \operatorname{argmin}_d \{\inf \mathcal{C}_{l_d}(d)\} \quad \text{where } d = 1 \text{ on } \mathcal{C} \subset \mathcal{B}. \quad (23)$$

To this end, the constitutive functions response by means of a global evolution system of regularized crack fracture gives rise to the global crack dissipation functional

$$\frac{d}{dt} \mathcal{C}_{l_d}(d) := \frac{1}{l_d} \int_{\mathcal{B}} [-g'(d_+) \mathcal{H} + \eta \dot{d}] \, dV = \int_{\mathcal{B}} \delta \gamma_l(d, \nabla d) \dot{d} \, dV \geq 0. \quad (24)$$

Here,  $\mathcal{H}$  is the so-called maximum crack driving force, see Section 2.3.3. The local evolution of the crack phase-field equation represented for the *third* PDE in the given domain  $\mathcal{B}$  resulting from (24) augmented with its homogeneous NBC, i.e.  $f(\alpha) \nabla d \cdot \mathbf{n} = 0$  on  $\partial \mathcal{B}$  yields

$$\eta_d \dot{d} = (1 - d) f(\alpha) \mathcal{H} - [f(\alpha) \omega'(d) - 2l_d^2 \operatorname{div}[f(\alpha) \cdot \nabla d]]. \quad (\text{F})$$

### 2.3. Constitutive equations

The coupled BVP is formulated through four specific fields (i.e., unknown solution fields) to illustrate the chemo-elasticity of lithium-ion battery electrode particles in the fracturing material by

$$\text{Global Primary Fields : } \mathfrak{U} := \{\mathbf{u}, d, c, \mu\}. \quad (25)$$

Here,  $\mathbf{u}$  is the displacement (mechanical deformation),  $c$  denotes the lithium concentration, and  $d$  is the crack phase-field ( $0 \leq d \leq 1$ ). The constitutive formulations for the hydraulic phase-field fracture are written in terms of the following set

$$\text{Constitutive State Variables : } \mathfrak{C} := \{\boldsymbol{\varepsilon}, \boldsymbol{\varepsilon}^c, d, \nabla d, \mathbb{B}\}, \quad (26)$$

representing a combination of a first-order gradient elasticity model and a first-order gradient damage model. A pseudo-energy density per unit volume is then defined as  $W := W(\mathfrak{C})$ , which is additively decomposed into an elastic contribution  $W_{elas}$ , and a Lithium-ion contribution  $W_{Li-ion}$  :

$$W(\mathfrak{C}) := W_{elas}(\boldsymbol{\varepsilon}, \boldsymbol{\varepsilon}^c, d) + W_{Li-ion}(c). \quad (27)$$

**2.3.1. Elasticity.** We illustrate the governing equations and variational formulation for the mechanical counterparts. Following the Coleman-Noll procedure [94], the stress tensor is obtained from the potential  $W_{elas}$  in (15) as

$$\boldsymbol{\sigma} = \frac{\partial W}{\partial \boldsymbol{\varepsilon}} = \frac{\partial W_{elas}}{\partial \boldsymbol{\varepsilon}} = g(d) \tilde{\boldsymbol{\sigma}}_+ + \tilde{\boldsymbol{\sigma}}_-, \quad (28)$$

where fractured and unfractured contributions of stress as are given by

$$\begin{aligned}\tilde{\boldsymbol{\sigma}}_+ &:= \frac{\partial \psi_e^+}{\partial \boldsymbol{\varepsilon}} = KH^+[I_1](\boldsymbol{\varepsilon}^e : \mathbf{I})\mathbf{I} + 2\mu\boldsymbol{\varepsilon}^{e,dev}, \\ \tilde{\boldsymbol{\sigma}}_- &:= \frac{\partial \psi_e^-}{\partial \boldsymbol{\varepsilon}} = K(1 - H^+[I_1])(\boldsymbol{\varepsilon}^e : \mathbf{I})\mathbf{I}.\end{aligned}\quad (29)$$

However, in this manuscript we use a hybrid method [95, 96] to have further acceleration in numerical implementation, so we have following:

$$\boldsymbol{\sigma} = \frac{\partial W}{\partial \boldsymbol{\varepsilon}} = \frac{\partial W_{elas}}{\partial \boldsymbol{\varepsilon}} = g(d)\tilde{\boldsymbol{\sigma}} \quad \text{with} \quad \tilde{\boldsymbol{\sigma}} = \tilde{\boldsymbol{\sigma}}_+ + \tilde{\boldsymbol{\sigma}}_-, \quad (30)$$

in which  $\boldsymbol{\sigma}$  is the standard linear elastic stress tensor, so  $\boldsymbol{\sigma} = K(\boldsymbol{\varepsilon}^e : \mathbf{I})\mathbf{I} + 2\mu\boldsymbol{\varepsilon}^{e,dev}$ .

The decoupled representation of the fourth-order elasticity tensor (to relate the work into conjugate pairs of stress and strain tensors) is obtained through the additive decomposition of the stress tensor, which reads as follows:

$$\mathbb{C} := \frac{\partial \boldsymbol{\sigma}(\boldsymbol{\varepsilon}, \boldsymbol{\varepsilon}^c, d)}{\partial \boldsymbol{\varepsilon}} = g(d) \frac{\partial \boldsymbol{\sigma}^+(\boldsymbol{\varepsilon}, \boldsymbol{\varepsilon}^c, d)}{\partial \boldsymbol{\varepsilon}} + \frac{\partial \boldsymbol{\sigma}^-(\boldsymbol{\varepsilon}, \boldsymbol{\varepsilon}^c, d)}{\partial \boldsymbol{\varepsilon}} =: g(d)\tilde{\mathbb{C}}^+ + \tilde{\mathbb{C}}^-, \quad (31)$$

with

$$\tilde{\mathbb{C}}^+ = KH^+(\nabla \cdot \mathbf{u})\mathbf{I} \otimes \mathbf{I} + 2\mu\mathbb{P}, \quad \text{and} \quad \tilde{\mathbb{C}}^- = K(1 - H^+(\nabla \cdot \mathbf{u}))\mathbf{I} \otimes \mathbf{I},$$

where the identity  $\partial_{e,\boldsymbol{\varepsilon}}\boldsymbol{\varepsilon}^{dev}(\mathbf{u}) =: \mathbb{P}$  is used.

**2.3.2. Lithium-ion concentration flow.** We describe the governing equations which will be used as a departing point to derive the variational formulation for the degradation mechanisms of lithium-ion concentration flow.

**Governing equations.** By employing the Coleman-Noll inequality condition in thermodynamics, the lithium chemical potential  $\mu$  is derived from the first-order derivative of the pseudo-energy density function  $W$  given in (27) by

$$\mu(\boldsymbol{\varepsilon}^e, c) \approx \mu(\boldsymbol{\varepsilon}, \boldsymbol{\varepsilon}^c, \Theta_L) := \frac{\partial W}{\partial c} = \mu_0 + R\vartheta \left( \ln \Theta_L - \ln(1 - \Theta_L) \right) - \Omega_c \sigma_h. \quad (32)$$

Here,  $\sigma_h$  is the hydrostatic stress that is  $\sigma_h = \frac{1}{3}tr(\boldsymbol{\sigma})$ . By means of (32) and (17) lithium-ion flux vector reads:

$$\mathbb{H} = -\mathbf{K}(c, d) \nabla \mu = -\frac{g(d)D}{1 - \Theta_L} c \left( \frac{\nabla c}{c} - \frac{\nabla N_L}{N_L} \right) + \frac{g(d)D}{R\vartheta} c \Omega_c \nabla \sigma_h. \quad (33)$$

Thus, we have the following:

$$\mathbb{H} = \mathbf{K}\mathbb{B} = -g(d)D \nabla c + \frac{g(d)D}{R\vartheta} c \Omega_c \nabla \sigma_h. \quad (34)$$

Employing the above-mentioned identity between lithium flux vector and lithium concentration field in addition to the (C), the conservation of mass takes the following form

$$\frac{c - c_n}{\tau} - \bar{r}_L - \text{Div}[\mathbb{H}] = \frac{c - c_n}{\tau} - \bar{r}_L + \text{Div}[D \nabla c] - \text{Div}\left[\frac{D}{R\vartheta} c \Omega_c \nabla \sigma_h\right] = 0. \quad (35)$$

**2.3.3. Damage.** To enforce the crack irreversibility condition, we define the history field by  $\mathcal{H}$  given in (F) which is the crack driving force and is derived through the maximum expression of the positive crack driving state function through:

$$\mathcal{H}(\boldsymbol{x}, t) := \max_{s \in [0, t]} \tilde{D}(\mathbf{C}(\boldsymbol{x}, s)). \quad (36)$$

Next, positive crack driving state function  $\tilde{D}$  for different cases of monothonic charge process and fatigue charge/discharge process will be explained.

- **Monotonic charge process** In the case of the monotonic charge process, the crack driving force  $\mathcal{H}$  given in (F), is derived through the maximum expression of the positive crack driving state function, through:

$$\tilde{D} := \frac{2c_d l_d}{g_c} \psi_e^+(I_1, I_2) \geq 0. \quad (37)$$

Here,  $g_c$  is Griffith's critical elastic energy release rate.

- **Fatigue charge/discharge process** In the case of the fatigue charge/discharge process, the crack driving force  $\mathcal{H}$

$$\tilde{D} := \frac{2c_d l_d}{f(\alpha) g_c} \psi_e^+(I_1, I_2) \geq 0. \quad (38)$$

In this case,  $g_c$  Griffith's critical elastic energy release rate is scaled by a non-negative fatigue degradation function  $f(\alpha)$ .

In the failure mechanism, the dissipation-potential density  $\hat{\Phi}_{frac}$  associated with the evolving crack topology is elaborated in the following. To this end, the formulation response needs to preserve thermodynamical consistency by ensuring an irreversibility condition, i.e.,  $\dot{d} \geq 0$ . To do so, dissipation-potential density for fracture evolution reads:

$$\hat{\Phi}_{frac}(\dot{d}, \nabla \dot{d}; \alpha) := g_c f(\alpha) \frac{d}{dt} \gamma(d, \nabla d). \quad (39)$$

Thus, reads:

$$\hat{\Phi}_{frac}(\dot{d}, \nabla \dot{d}) \geq 0. \quad (40)$$

Here, we assumed non-negative fatigue degradation function following [97] as:

$$f(\alpha) = \begin{cases} 1 & \alpha(\boldsymbol{x}, t) \leq \alpha_c \\ [1 - k_f \log \frac{\alpha(\boldsymbol{x}, t)}{\alpha_c}]^2 & \alpha(\boldsymbol{x}, t) \leq \alpha_c 10^{1/k_f} \\ 0 & \text{otherwise} \end{cases} \quad (41)$$

where,  $\alpha_c \geq 0$  is a material threshold parameter, which below so that no fatigue effects are triggered. Also,  $k_f$  is fatigue model parameter. Figure (4) delivers a fatigue degradation function  $f(\alpha)$  given in (41). It is trivial by varying the fatigue model parameter  $k_f$  the slop of the the  $f(\alpha)$  could be turned, so helping to have more calibration when simulating material modeling. The fatigue variable  $\alpha$  is defined as an accumulation of strain energy density  $W_{elas}$  during loading stages, thus:

$$\alpha(\boldsymbol{x}, t) := \int_0^t \dot{\Lambda}(\boldsymbol{x}, s) \bar{H}(\dot{\Lambda}(\boldsymbol{x}, s)) dA \quad \text{with} \quad \Lambda(\boldsymbol{\varepsilon}^e, \mu, d) := W_{elas}(\boldsymbol{\varepsilon}, \boldsymbol{\varepsilon}^c, d), \quad (42)$$

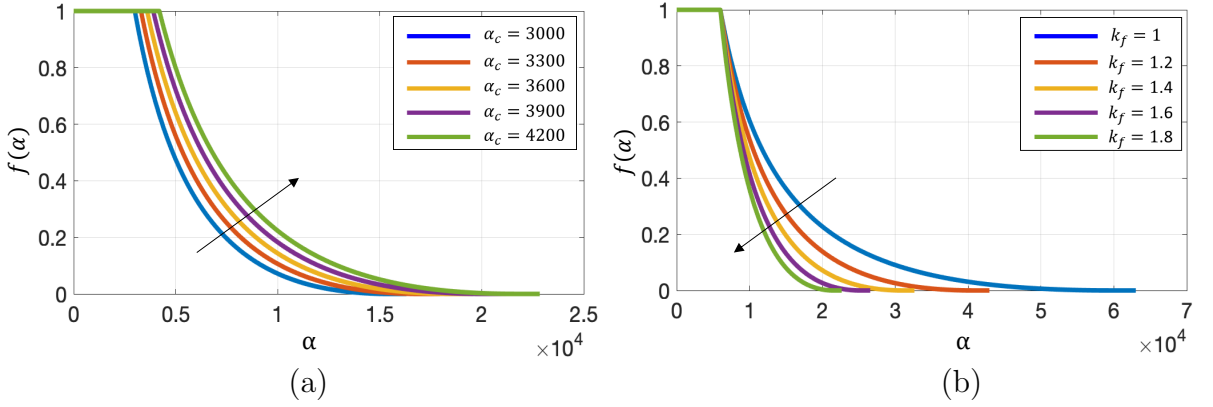


**Figure 4:** Fatigue degradation function (a) for different values of fatigue threshold parameter  $\alpha_c$  at fixed  $k_f = 1.4$  and (b) different values for fatigue model parameter  $k_f$  at fixed  $\alpha_c = 3000$ .

that is

$$\alpha(\mathbf{x}, t) = \alpha_n(\mathbf{x}, t) + (\Lambda - \Lambda_n)\bar{H}(\Lambda - \Lambda_n). \quad (43)$$

Here,  $\bar{H}$  refers to the standard Heaviside function.

#### 2.4. Variational formulations derived for the coupled multi-field problem

In this section, by having all the governing equations and strong forms for all three fields, i.e.,  $(\mathbf{u}, c, d)$ , and  $\mu$  based on the constitutive equation given in (32), we could able to derive the variational formulations derived for the coupled multi-field problem.

**Elasticity contribution.** The variational formulation with respect to the displacement field derived through the global mechanical PDE given (E) yields

$$\begin{aligned} \Pi_{\mathbf{u}}(\mathbf{\Upsilon}; \delta \mathbf{u}) &= \int_{\mathcal{B}} [\delta \boldsymbol{\varepsilon}(W_{elast} + W_{Li-ion}) : \boldsymbol{\varepsilon}(\delta \mathbf{u})] \, dV \\ &= \int_{\mathcal{B}} [\boldsymbol{\sigma} : \boldsymbol{\varepsilon}(\delta \mathbf{u}) - \bar{\mathbf{f}} \cdot \delta \mathbf{u}] \, dV - \int_{\partial \mathcal{B}_N^u} \bar{\mathbf{r}} \cdot \delta \mathbf{u} \, dA = 0 \quad \forall \delta \mathbf{u} \in \mathcal{W}_0^u, \end{aligned} \quad (E)$$

which corresponds to the weak form of the mechanical balance equations, which  $\mathcal{W}_0^u$  denotes the function space for the virtual displacement fields, i.e., with homogeneous kinematic boundary conditions. We note that in (E), the Cauchy stress tensor  $\boldsymbol{\sigma}$  is given in (28).

**Lithium-ion concentration contribution.** The weak formulation with respect to the conservation of lithium-ion concentration derived through the global mass conservation for the lithium concentration PDE given (35) reads

$$\begin{aligned} \Pi_c(\mathbf{\Upsilon}, \delta c) &= \int_{\mathcal{B}} \left[ ((c - c_n) - \tau \bar{r}_F) \delta c + (\tau \mathbf{K} \mathbb{B}) \cdot \delta \nabla c \right] dV \\ &\quad + \int_{\partial_N^c \mathcal{B}} \tau \bar{H} \delta c \, dA = 0, \quad \forall \delta c \in \mathcal{W}_0^c, \end{aligned} \quad (C)$$

which is based on the lithium concentration field. Here, the concentration diffusivity  $\mathbf{K}$  is given in (18), where the reduced form of the lithium-ion flux vector, i.e.,  $\mathbb{H} = \mathbf{K} \mathbb{B}$ , given in (34).

**Fracture contribution.** Finally, the weak formulation with respect to the crack phase-field is derived through the local evolution of the crack phase-field equation given (F) becomes:

$$\Pi_d(\mathbf{U}; \delta d) = \int_{\mathcal{B}} \left[ \left( (1-d)\mathcal{H} - \omega'(d) + \frac{\eta_d}{\tau}(d - d_n) \right) \delta d - l_d^2 \nabla d \cdot \nabla(\delta d) \right] dV = 0 \quad (\text{F})$$

$$\delta d \in \mathcal{W}^d.$$

Here, the crack driving force  $\tilde{D}$  for the case of the monothonic charge process is given in (37), and in the case of the fatigue charge/discharge process shown in (38).

The fully coupled variational multi-field problem to describe mechanically induced fatigue fractures in chemo-elasticity media is formulated in (E)-(C)-(F). Thus, the following equation associated with finite time increment  $[t_n, t_{n+1}]$  has to be solved. To do so, we need to find, the global primary fields at time  $t_{n+1}$  for  $\mathbf{u} := \mathbf{u}_{n+1} \in \mathcal{W}_0^u$ ,  $c := c_{n+1} \in \mathcal{W}_0^c$ , and  $d := d_{n+1} \in \mathcal{W}_{d_{n-1}}^d$  as the solution of the following incremental coupled problem:

$$\Pi(\mathbf{U}, \delta \mathbf{U}) = \underbrace{\Pi(\mathbf{U}, \delta \mathbf{u})}_{(\text{E})} + \underbrace{\Pi(\mathbf{U}, \delta c)}_{(\text{C})} + \underbrace{\Pi(\mathbf{U}, \delta d)}_{(\text{F})} = 0 \quad \forall (\delta \mathbf{u}, \delta c, \delta d) \in (\mathcal{W}_0^u, \mathcal{W}_0^c, \mathcal{W}^d). \quad (44)$$

In order to solve the chemo-mechanical coupled with phase-field fracture system (44), we first solve (E)-(C) equations monolithically (simultaneously obtaining  $(\mathbf{u}, c)$ ). Then, a staggered approach is used to obtain the phase-field fracture  $d$  by means of (F). To that end, we fix alternately  $(\mathbf{u}, c)$  and estimate  $d$  and vice versa. The procedure is continued until convergence, using given  $\text{TOL}_{\text{Stag}}$ :

$$\text{Res}_{\text{Stag}}^k \leq \text{TOL}_{\text{Stag}}, \quad (45)$$

with

$$\text{Res}_{\text{Stag}}^k := |\Pi_\varepsilon^\tau(\mathbf{u}_k, c_k, d_k; \delta \mathbf{u})| + |\Pi_\mu(\mathbf{u}_k, c_k, d_k; \delta \mu)| + |\Pi_d(\mathbf{u}_k, c_k, d_k; \delta d)| \leq \text{TOL}_{\text{Stag}},$$

$$\forall (\delta \mathbf{u}, \delta \mu, \delta d) \in (\mathcal{W}_0^u, \mathcal{W}_0^\mu, \mathcal{W}^d). \quad (46)$$

This is a common way for solving multi-field phase-field approach [98, 99]. We outline a solution procedure of the fatigue failure of the lithium-Ion battery in Algorithm 1.

### 3. Numerical examples

This section demonstrates the performance of the proposed fatigue failure theory for lithium diffusion induced fracture in lithium-ion battery electrode particles. Different boundary value problems are investigated, in which the electrode particles with built-in micro defects/cavities in the form of initial cracks and pores are considered. In order to assess the influence of these defects on the crack behavior, and specifically the lifetime of the battery, the distribution, size and number of defects are varied. The crack behavior is analyzed from qualitative results, such as the crack pattern, but also from quantitative

**Algorithm 1** The staggered iterative solution process for (44) at a fixed time-step  $n$ .

**Input:** loading data  $(\bar{\mathbf{f}}, \bar{\mathbf{t}}_n)$  on  $\mathcal{C}$  and  $\Gamma_N$ , respectively;

solution  $(\mathbf{u}_{n-1}, c_{n-1}, d_{n-1})$  from step  $n - 1$ .

Initialization,  $k = 1$ :

- set  $(\mathbf{u}_0, c_0, d_0) := (\mathbf{u}_{n-1}, c_{n-1}, d_{n-1})$ .

Staggered iteration between  $(\mathbf{u}, c)$  and  $d$ :

- solve following system of equations in a monolithic manner given  $d_{k-1}$ ,

$$\begin{cases} \int_{\mathcal{B}} [\boldsymbol{\sigma} : \boldsymbol{\varepsilon}(\delta \mathbf{u}) - \bar{\mathbf{f}} \cdot \delta \mathbf{u}] \, dV - \int_{\partial \mathcal{B}_N^u} \bar{\boldsymbol{\tau}} \cdot \delta \mathbf{u} \, dA = 0, \\ \int_{\mathcal{B}} [((c - c_n) - \tau \bar{r}_F) \delta c + (\tau \mathbf{K} \mathbb{B}) \cdot \delta \nabla c] \, dV + \int_{\partial_N^c \mathcal{B}} \tau \bar{H} \delta c \, dA = 0, \end{cases}$$

for  $(\mathbf{u}, c)$ , set  $(\mathbf{u}, c) =: (\mathbf{u}_k, c_k)$ ,

- given  $(\mathbf{u}_k, c_k, \alpha_k)$ , compute crack driving force:  $\tilde{D} := \frac{2c_d l_d}{\beta g_c} \psi_e^+(I_1, I_2) \geq 0$  for  
monotonic:  $\beta = 1$ , and fatigue:  $\beta = f(\alpha)$  see (41)

with

$$\alpha(\mathbf{x}, t) = \alpha_k(\mathbf{x}, t) + (\Lambda - \Lambda_n) \bar{H}(\Lambda - \Lambda_n)$$

- given  $(\mathbf{u}_k, c_k)$ , solve fatigue fracture problem by

$$\int_{\mathcal{B}} \left[ \left( (1-d)\mathcal{H} - d + \frac{\eta_d}{\tau} (d - d_n) \right) \delta d - l_d^2 \nabla d \cdot \nabla(\delta d) \right] \, dV = 0$$

for  $d$ , set  $d =: d_k$ ,

- for the obtained pair  $(\mathbf{u}_k, c_k, d_k)$ , check staggered residual by:  $\text{Res}_{\text{Stag}}^k$
- if fulfilled, set  $(\mathbf{u}_k, c_k, d_k) =: (\mathbf{u}_n, c_n, d_n)$  then stop;
- else  $k + 1 \rightarrow k$ .

**Output:** solution  $(\mathbf{u}_n, c_n, d_n)$  at  $n^{\text{th}}$  time-step.

results, such as the fracture volume, fatigue degradation function and the accumulative bulk energy functional.

Here, we considered two loading cases that is monothonic charge process, and the fatigue charge/discharge process. In the first case, the concentration at the electrode particle boundary is monotonically increased with an increment of  $\Delta c = 1000 \text{ mol/m}^3$  up to the maximum concentration of  $c_{max} = 1.5 \times 10^6 \text{ mol/m}^3$ . Next, a cyclic concentration load is applied to the same geometry, see Figure 6. In general, we have a free boundary condition for the displacement in all directions and the phase-field variable was set equal to 1 at pre-defined cracks.

The material parameters [18] are listed in Table 1. Since, here a rate-dependent problem is considered, for the time increment of the monotonic charge process, we set  $\Delta t_{mono} = 0.125 \text{ s}$ , while for the cyclic charge/discharge process, we set  $\Delta t_{cyc} = 200 \text{ s}$ .

**Space discretization.** In the numerical simulations, the global primary variables are discretized using finite element basis functions, with linear triangular  $T_1$  elements for the two-dimensional problems, and trilinear hexahedral  $H_1$  elements for the three-dimensional problems.

**Model parameters.** For the stability, an artificial residual stiffness is introduced and set to  $\kappa_d = 1 \times 10^{-8}$ . The length scale is defined as  $l_d = 2h_{min}$ , where  $h_{min}$  is the smallest element size.

**Solution of the linear/nonlinear problems.** Linear solvers are used to solve the displacement  $u(x, t)$  and the phase-field variable  $d(x, t)$ , while the concentration  $c(x, t)$  is solved with a non-linear solver. The matrix type is managed by the *multifrontal massively parallel sparse* direct Solver package (MUMPS), which is well suited for distributed matrices and systems with huge numbers of degrees of freedom. For a more detailed discussion, see [100, 101].

**Software.** The implementation is based on FEniCS and the imported mesh is created via GMSH 4.10.4. The FEniCS docker container already includes MPICH and is fundamentally developed for parallel processing on laptops, workstations and also HPC clusters. The user can define the PDEs in Python that FEniCS translates via `ffc` into a low-level C code, enabling the compilation of highly efficient simulations. The cluster is managed by LUIS HPC cluster is SLURM 22.05.3.

### 3.1. Example 1: Lithium diffusion induced crack driven for a single notch

In the first numerical example, the cracking behavior of the electrode particle with an initial notch located in the center of the particle is investigated. In the first example, the radius of the electrode particle is  $r = 6 \times 10^{-5} \text{ mm}$ . Also, the length of the initial crack is  $C_1 = 3 \times 10^{-5} \text{ mm}$ , see Figure 5(a). The number of triangular elements is 24000.

The evolution of the cracks and qualitative  $y$ -displacement are shown in Figure 7. It can be seen that the crack volume grew primarily from the initial crack. In addition, crack nucleates form on the opposing boundary until they merge with the initial notch. The evolution of the corresponding crack volume and accumulative elastic energy are shown in Figure 8. Looking at the increasing crack column, it can be said that the full failure is reached before 500 s. Accordingly, the accumulated elastic energy increases until it drops rapidly in the fully broken state.

**Table 1:** Material/model parameters used in the numerical examples based on [18]

No.	Parameter	Name	Value	Unit
1.	$K$	Bulk modulus	77.5	GPa
2.	$\mu$	Shear modulus	35.77	GPa
3.	$D$	Lithium diffusion coefficient	$7.08 \times 10^{-15}$	$\text{m}^2 \cdot \text{s}^{-1}$
4.	$R$	Universal Gas constant	8.314	$\text{J} \cdot \text{K}^{-1} \cdot \text{mol}^{-1}$
5.	$\Omega_c$	Partial molar volume of lithium	$2.4 \cdot 10^{-6}$	$\text{m}^3 \times \text{mol}^{-1}$
6.	$N_L$	Number of moles of lattice sites	$6.022 \times 10^{23}$	$\text{mol}^{-1}$
7.	$\vartheta$	Ambient temperature	300	K
8.	$g_c$	Griffith's energy release rate	1	MPa · mm
9.	$\zeta$	Scaling factor	1	—
10.	$\eta_d$	Fracture viscosity	$10^{-6}$	$\text{N}/\text{m}^2\text{s}$
11.	$\kappa_d$	Stabilization parameter	$10^{-8}$	MPa
12.	$l_f$	Fracture length-scale	$5 \times 10^{-6}$	mm
13.	$k_f$	Fatigue model parameter	0.5	mm
14.	$\alpha_c$	Fatigue threshold parameter	$3.333 \times 10^3$	mm
15.	$c_0$	Initial concentration	300	$\text{mol} \cdot \text{m}^{-3}$
16.	$\Delta t$	Time increment	200	s

Figure 9 shows the normalized lithium concentration  $c/c_{max}$  as well as hydrostatic stress  $\sigma_h$  for all the examples at the complete failure. Example 1 shows that the concentration is lowest along the crack and, as expected, highest on the electrode particle surface. The hydrostatic stress is also lowest at the location of the crack. The highest stresses occur on the non-fractured electrode particle surface.

In the case of the cyclic charge/discharge process, the lithium concentration reaches a maximum value of  $c_{max} = 510000 \text{ mol/m}^3$  with an increment of  $\Delta c = 170000 \text{ mol/m}^3$ , see Figure 6. The resulting evolution of the crack phase-field  $d$  and normalized lithium concentration  $c/c_{max}$  are shown in Figure 10. In contrast to the monotonic loading case, it can be observed that the secondary that cracks develop at the boundary are more pronounced while they propagate towards merging with the primal crack initiated from the pre-defined notch initial notch. Furthermore it can be observed that the lithium concentration is lowest along the cracks.

The evolution of the corresponding crack volume and fatigue degradation functions are shown in Figure 11. Accordingly, the accumulated elastic energy is depicted in Figure 12. The fatigue degradation function indicates that the battery electrode exhibits softening as the cyclic load progresses. In addition, a less abrupt but gradually increasing crack volume can be observed compared to the monotonic load case. This is a sign of slow and less abrupt crack propagation, which can be expected in fatigue fracture. This finding also applies to the accumulative elastic energy.

### 3.2. Example 2: Lithium diffusion-induced crack driven for single notch with distributed cavities

Next, in the second example, in addition to the pre-defined crack in the electrode particle, multiple micro cavities (pores) are randomly distributed, see Figure 5. Here, we essentially aim, to investigate the impact of micro cavities on the crack pattern, which

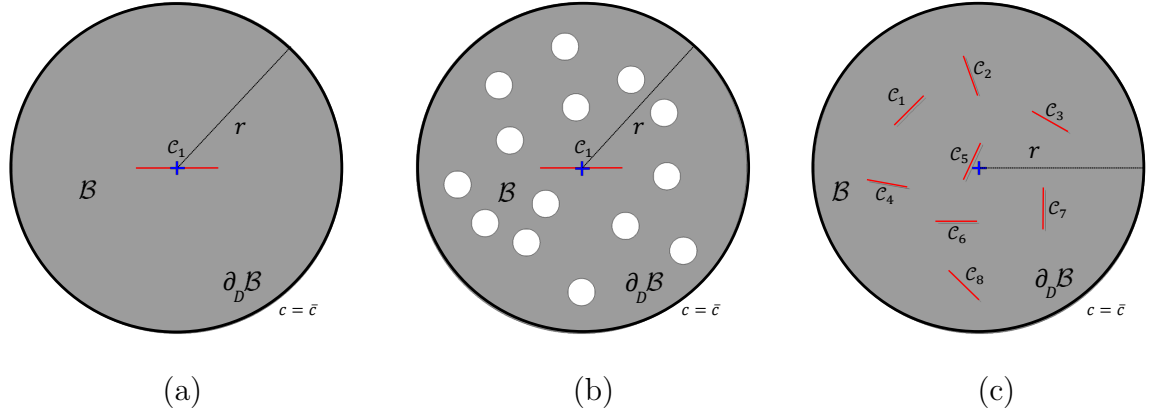


**Figure 5:** The representation of the geometry and boundary conditions for (a) Example 1, (b) Example 2, and (c) Example 3.

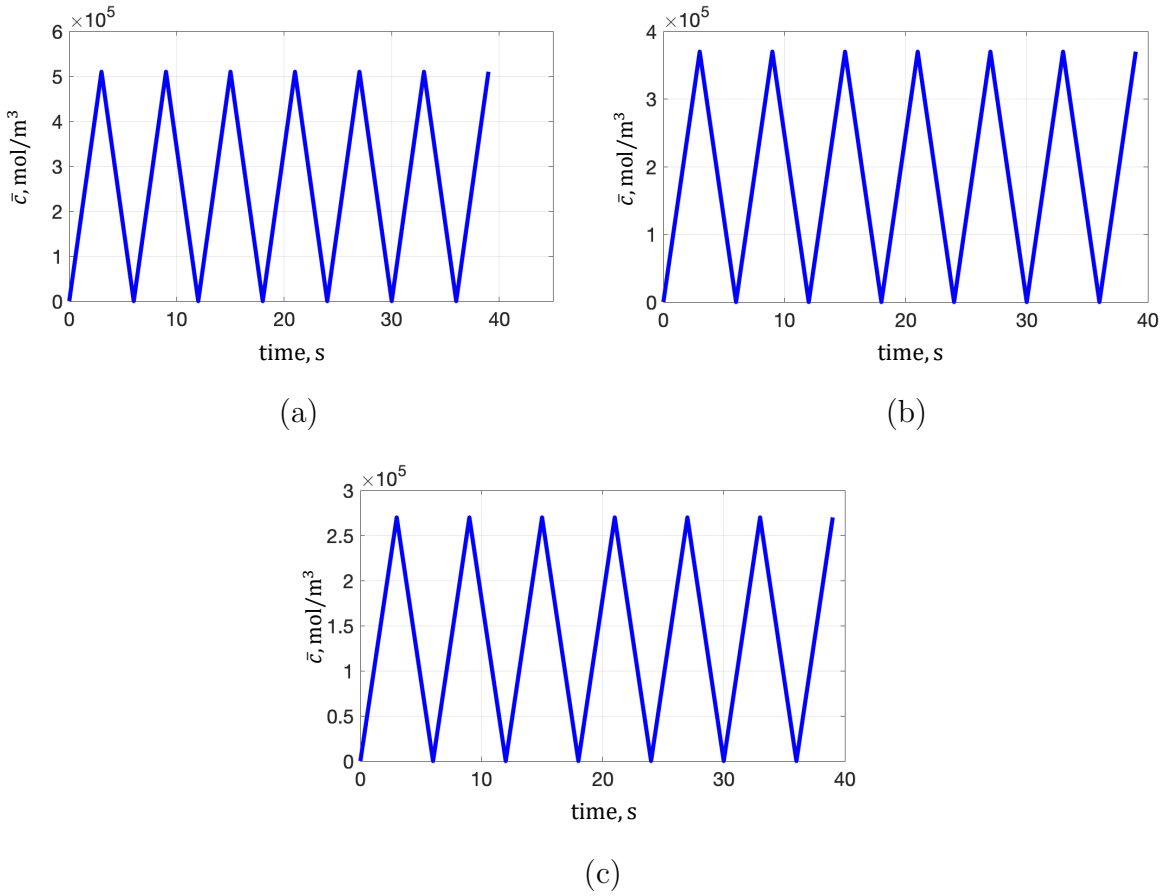


**Figure 6:** The representation of the cyclic charge/discharge process of the (a) Example 1, (b) Example 2, and (c) Example 3.

results in a reduction of the lifespan of battery. In this example, the radius of the electrode particle is  $r = 6 \times 10^{-5}$  mm, with a pre-defined notch allocated in the center of particle with a length of  $\mathcal{C}_1 = 3 \times 10^{-5}$ , same as the first example. Here, the circular pores have a radius of  $r_1 = 5 \times 10^{-6}$ . The number of triangular elements is 23300.

The evolution of the crack pattern and qualitative  $y$ -displacement are shown in Figure

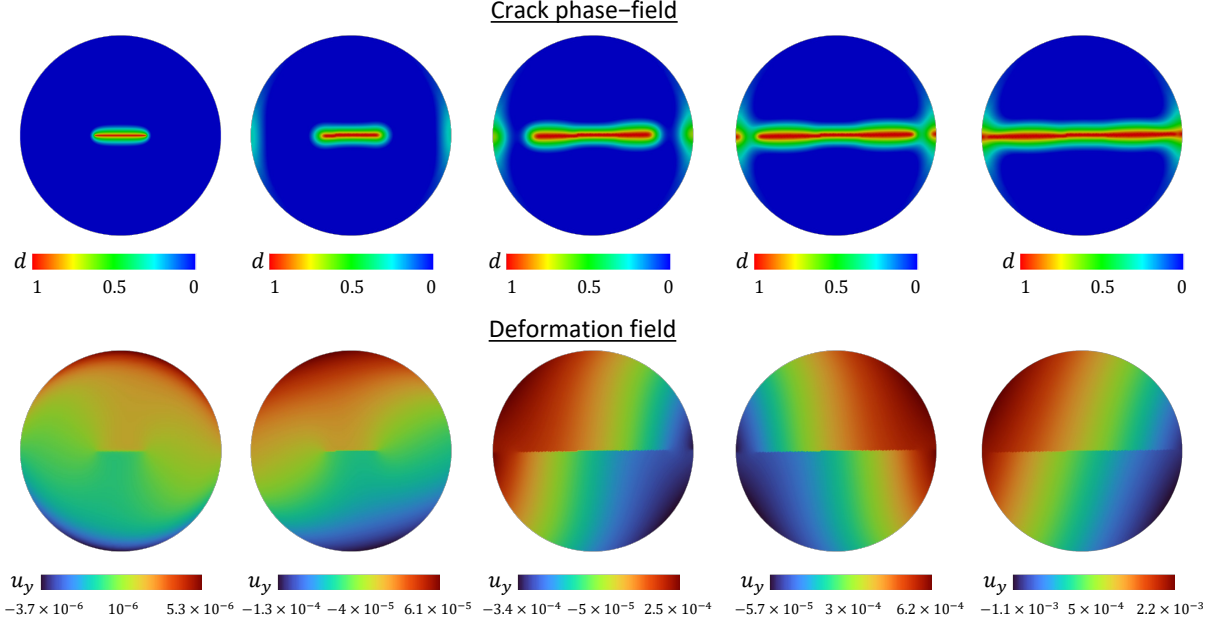


**Figure 7:** Example 1 (monotonic lithiation). Development of the crack phase-field in electrode particles and different deformation stages up to complete failure.

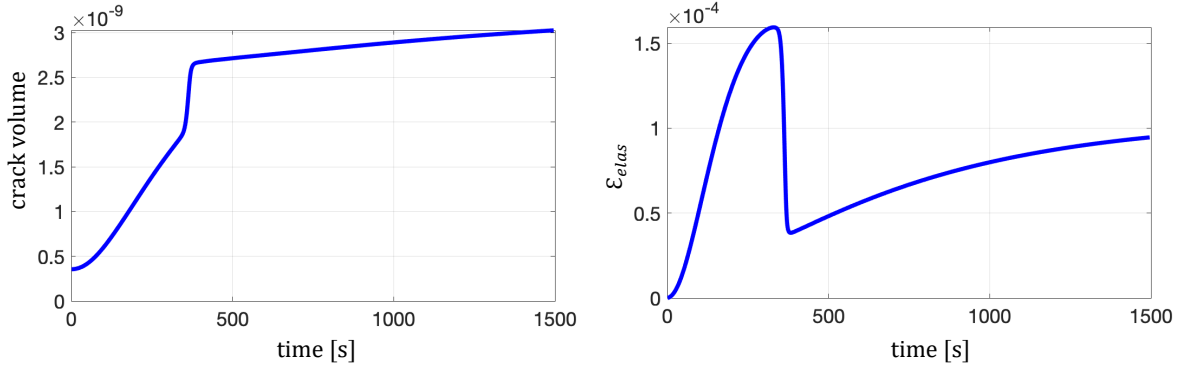


**Figure 8:** Example 1 (monotonic lithiation). Evaluation of the fracture volumes and bulk energy functional for an arbitrary Gaussian integration point for electrode particles.

13. The cracks develop initiating from the pre-defined crack and merging toward pores. It is trivial that the now larger pores redirect the crack path or even initiate secondary cracks compared to Example 1. Additionally, the crack volumes and the accumulated elastic energy behave similarly compared to Example 1, whereby the drop in elastic energy and thus the full failure occurs earlier, see Figure 14. Accordingly, Figure 9(b) depicts the hydrostatic stress at the complete failure such that the highest hydrostatic stress is observed at the pore surface oriented towards the center. Meanwhile, this is observed that the lowest hydrostatic stress is around the crack.

In the case of the fatigue charge/discharge process, the electrode particle surface is cyclically charged with a concentration increment  $\Delta c = 123333 \text{ mol/m}^3$  to the maximum concentration of  $c_{max} = 370000 \text{ mol/m}^3$  and the discharged back to the initial concentration, see Figure 6. The corresponding evolution of the crack phase-field and normalized lithium concentration  $c/c_{max}$  distribution are shown in Figure 15. Firstly, it is interesting

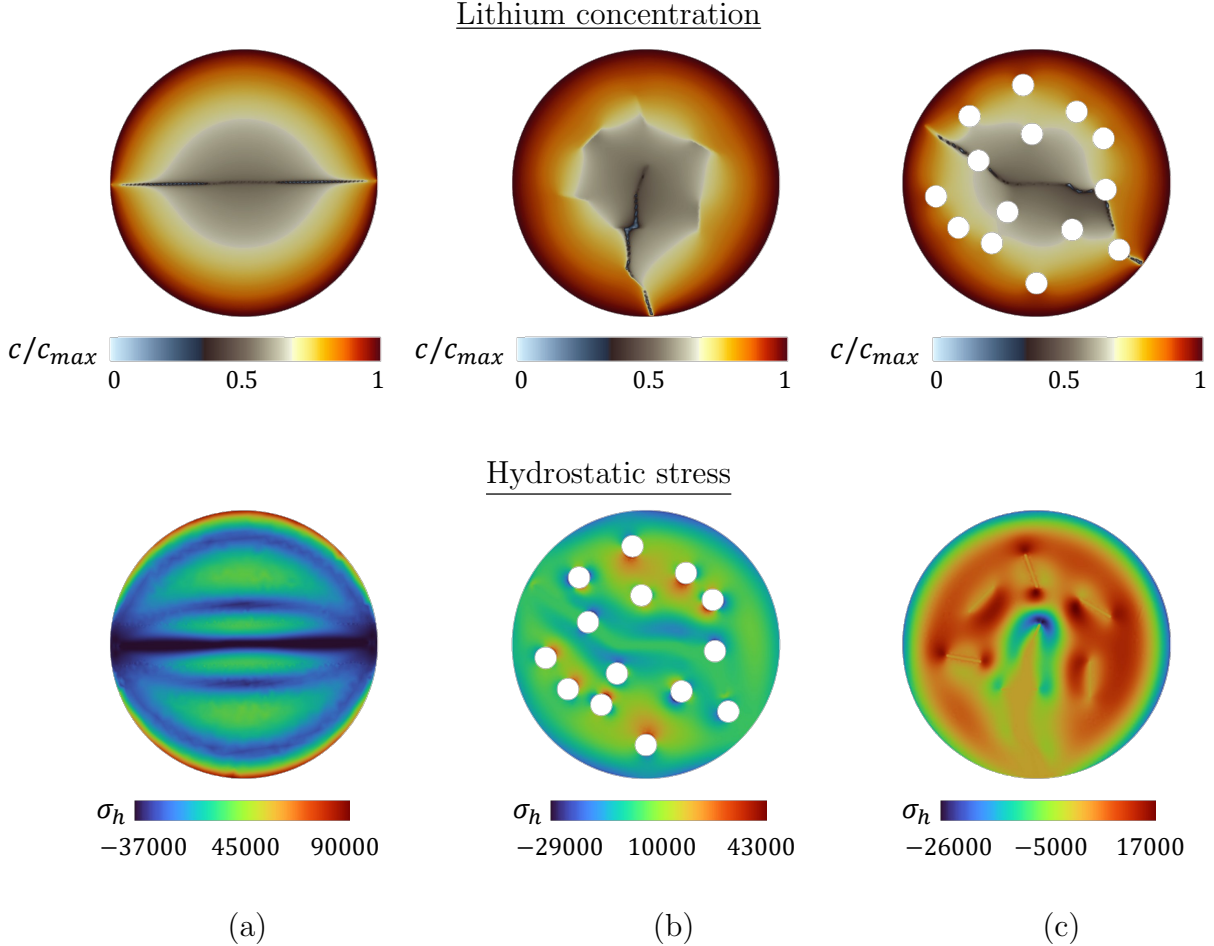


**Figure 9:** The representation of the Lithium concentration field  $c$  and hydrostatic stress  $\sigma_h$  at fully fractured state for (a) Example 1, (b) Example 2, and (c) Example 3.

to note that the change from monotonic to cyclic loading leads to a new crack pattern, in which branching can also be observed. Furthermore, in contrast to the monotonic case, additional crack nucleation at the pores is observed. However, not all of them show crack growth in the further progress of the fracture evolution.

The respective crack volumes and fatigue degradation functions are shown in Figure 16. Additionally, the accumulated elastic energy is depicted in Figure 17. It is trivial, after 2000 cycles, the crack volume as well as accumulated elastic energy reached to the stable region, meaning no further crack propagation could be expected.

It can be grasped that, since each cycles for lithiation and delithiation requires four-way to complete therefore, each cycle will take  $4 \times \delta T = 800$  s. Thus, in this for fatigue test, we could observe that after 15000 cycles complete failure has been reached, see Figure 17, and crack growth becomes stable, see Figure 16. Thus a final failure took  $800 \times 415000 = 12,000,000$  s, which results in a reduction of the effective amount of active material (with in crack area).

Additionally, for the monotonic lithiation test, approximately after 1000 steps, we reach to the complete failure, see Figure (14). This means when lithiation around the

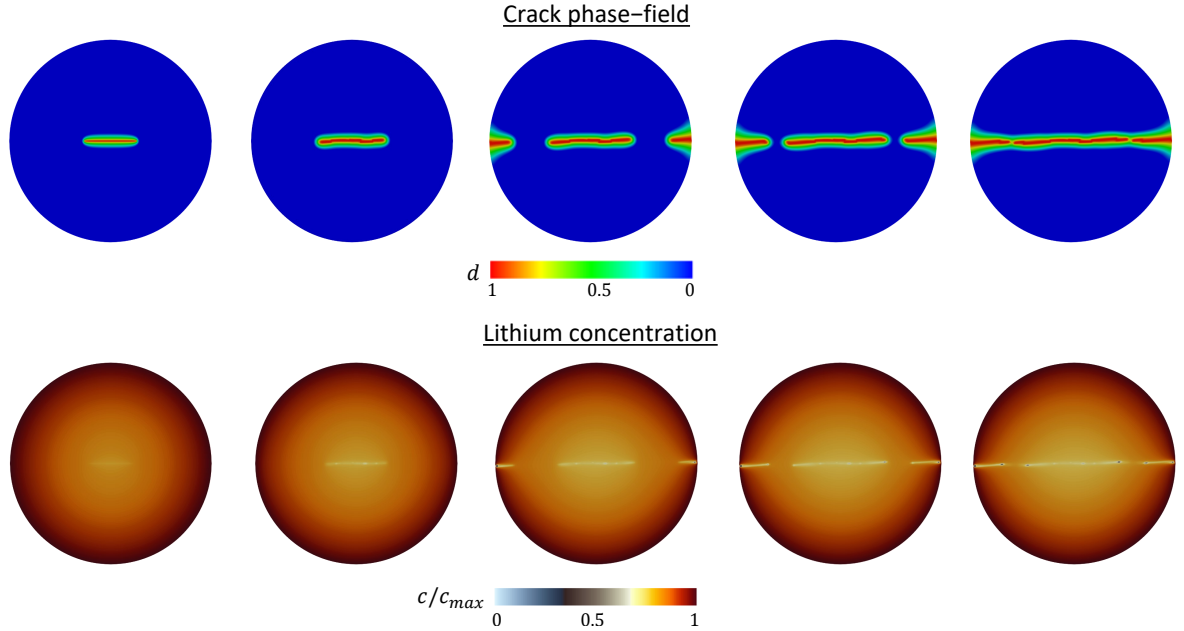


**Figure 10:** Example 1 (cyclic lithiation/delithiation). Development of the crack phase-field in electrode particles and different lithium concentration up to complete failure.

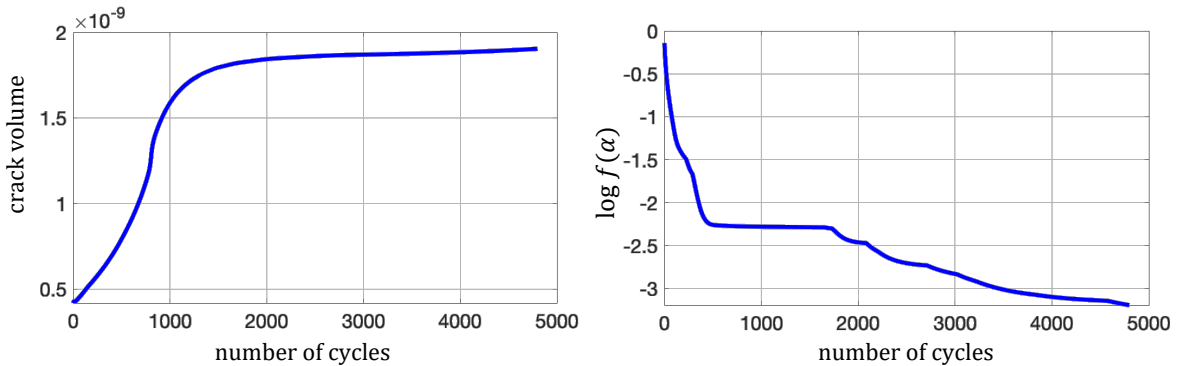


**Figure 11:** Example 1 (cyclic lithiation/delithiation). Evaluation of the fracture volumes and fatigue degradation functions for an arbitrary Gaussian integration point for electrode particles.

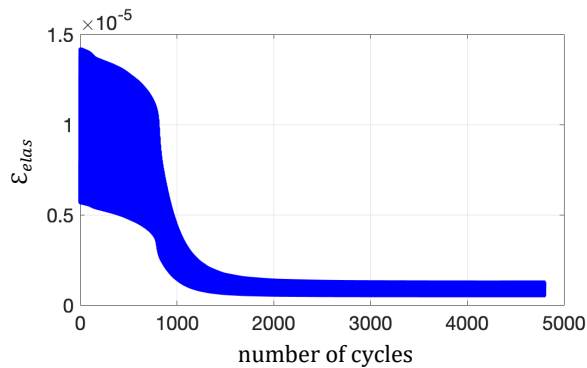


**Figure 12:** Example 1 (cyclic lithiation/delithiation). The accumulated elastic energy functional with respect to the number of cycles.

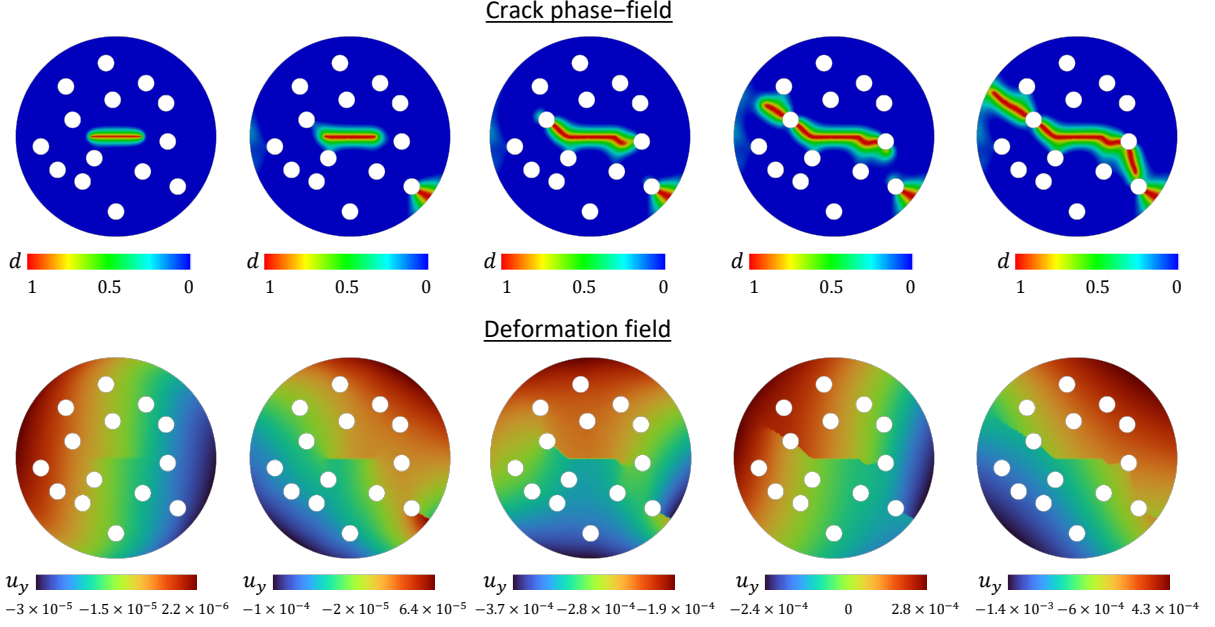


**Figure 13:** Example 2 (monotonic lithiation). Development of the crack phase-field in electrode particles and different deformation stages up to complete failure.

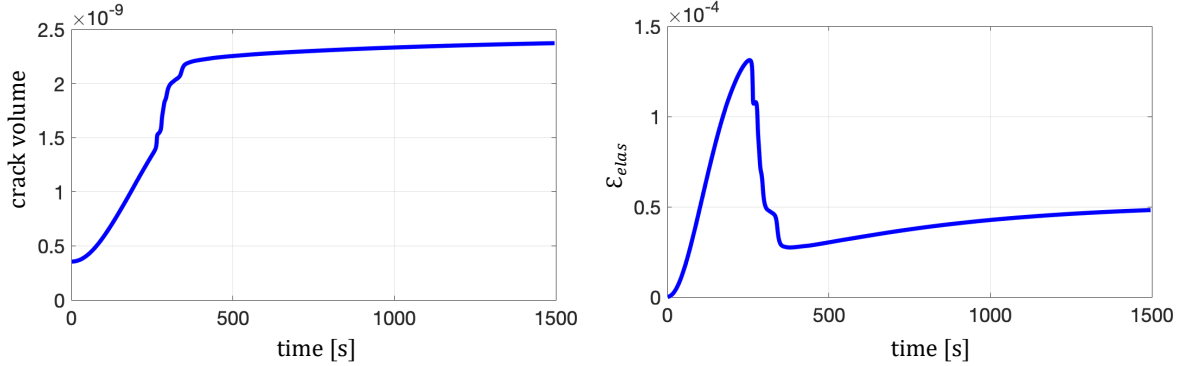


**Figure 14:** Example 2 (monotonic lithiation). Evaluation of the fracture volumes and bulk energy functional for an arbitrary Gaussian integration point for electrode particles.

boundary reached to the  $300,000 \text{ mol} \cdot \text{m}^{-3}$  on  $\partial_D^c \mathcal{B}$  which is equivalent to the  $300\delta T = 60,000 \text{ s}$ , we have complete failure. Accordingly, this influences the overall capacity and efficiency of the battery, therefore the efficiency of the battery declines as function of time.

Nevertheless, the current analysis, which shows the degradation of the electrode particle with respect to time, it gives crude estimate for the battery life. It is also perhaps one can do further investigation on the fatigue studies by basically looking at S-N curves. This area for further investigation remains as an open question.

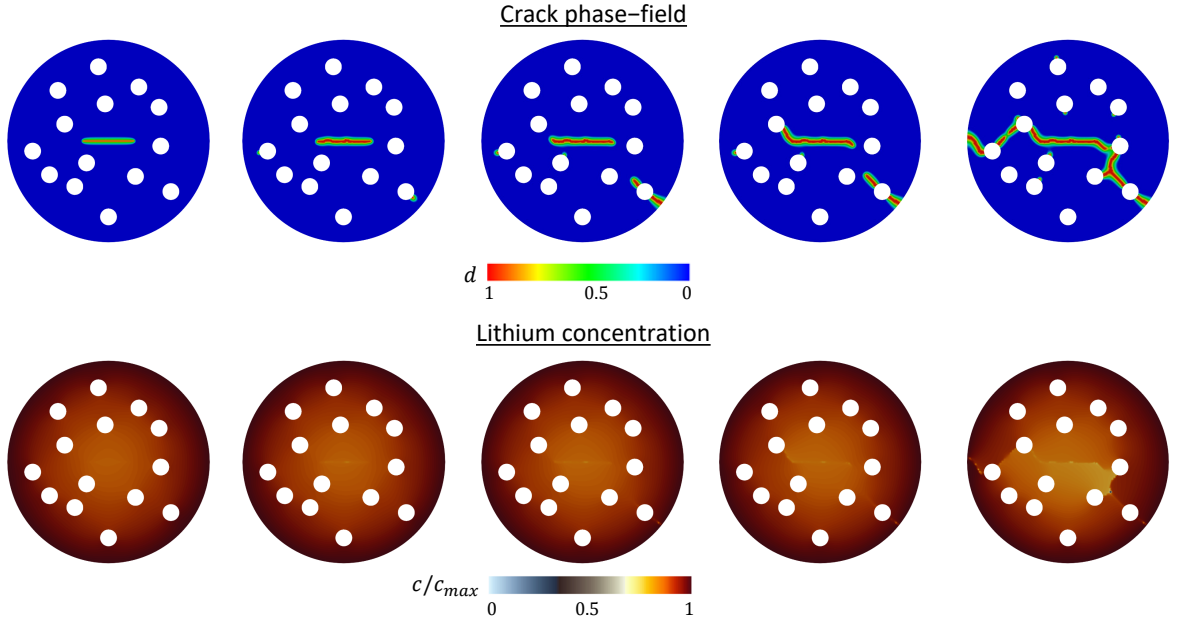


**Figure 15:** Example 2 (cyclic lithiation/delithiation). Development of the crack phase-field in electrode particles and different lithium concentration up to complete failure.

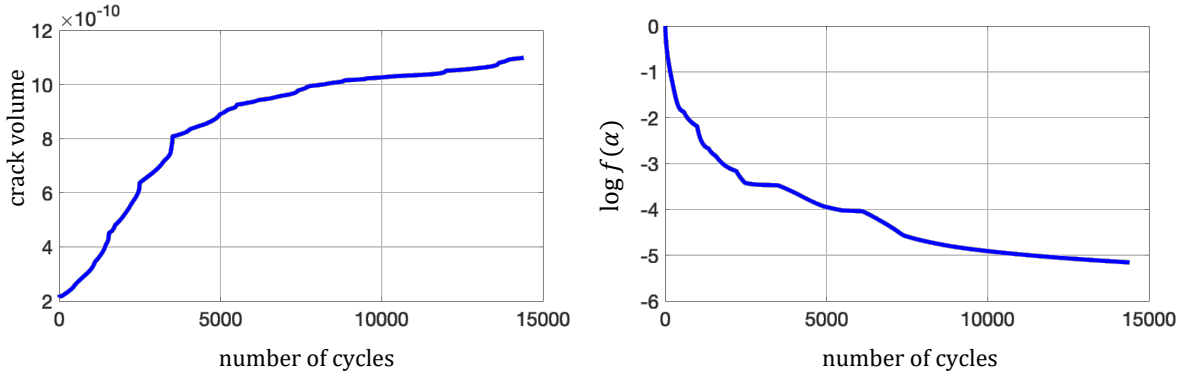


**Figure 16:** Example 2 (cyclic lithiation/delithiation). Evaluation of the crack volumes and fatigue degradation functions for an arbitrary Gaussian integration point for electrode particles with different aspect ratios.

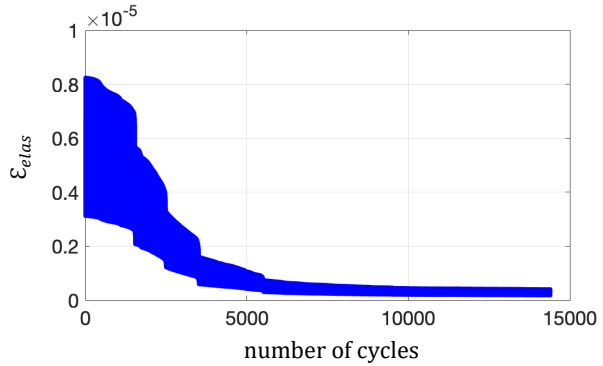


**Figure 17:** Example 2 (cyclic lithiation/delithiation). The accumulated elastic energy functional with respect to the number of cycles.

### 3.3. Example 3: Lithium diffusion-induced crack driven for multiple distributed notches

In the third example, we investigate at the influence of multiple randomly distributed predefined cracks to the lifetime of the lithium-ion battery, see Figure 5. In this example, the radius of the electrode particle is  $r = 6 \times 10^{-5}$  mm, identical to other examples. Here, we allocated 8 initial cracks of length  $\mathcal{C} = 1.5 \times 10^{-5}$  mm. The number of triangular elements is approximately 245 000.

The formation of the crack patterns and the qualitative  $y$ -displacement are shown in Figure 18. It has been observed that first the crack initiation as well as propagation occurs near the boundary, which then merges with the other notches. Finally, at the end of failure the crack branching is also observed.

In Figure 19 the crack volume and the elastic energy of Example 3 are shown. The elastic energy displays several pronounced maximal points. This is due to the fact that the crack growth only progresses in stages, so the elastic energy is only partially reduced and can increase due to further lithiation until the next crack propagates. As a result, secondary fracture, and crack branching were observed. The lithium concentration is lowest especially along and also between cracks, this can be observed in Figure 9. It has been observed that a high lithium concentration accumulates close to the crack tip, which is due to the high hydrostatic stresses  $\sigma_h$  appearing near the crack tip.

In the fatigue case, the electrode particles are cyclically loaded at the boundary with a lithium concentration increment  $\Delta c = 86666$  mol/m<sup>3</sup> to  $c_{max} = 260000$  mol/m<sup>3</sup> and unloaded again to the initial concentration, see Figure 6. The evolution of the crack phase-field, and normalized lithium concentration within electrode particles are shown in Figure 20. The crack path shows similarities with that of the monotonic case, but exhibits branching at two locations at the end of the failure. The mathematical framework is therefore also able to simulate complex phenomena, such as merging and branching of cracks. Again, the concentration is lowest especially along and between cracks.

The crack volumes, fatigue degradation functions, as well as the accumulated elastic energy of the fatigue charge/discharge process are depicted in Figures 21 and 22. Accordingly, the material exhibits softening and a drop in elastic energy caused by the crack. This is inline with Examples 1 and 2.

### 3.4. Example 4: Three-dimensional Lithium diffusion-induced crack driven for randomly distributed cavities

In the last example, we finalize this section by investigating the results achieved through the proposed model in the three-dimensional setting at a glance. Here, lithium diffusion-induced crack driven for multiple distributed notches is considered, see Figure 23. In this example, the radius of the electrode particle is  $r = 6 \times 10^{-5}$  mm, identical to two-dimensional examples. Here, we have 8 randomly distributed circular cracks allocated with a radius of  $r_1 = 7.5 \times 10^{-6}$  mm, so  $\mathcal{C} = 1.76 \times 10^{-10}$  mm<sup>2</sup>. In this example, the electrode particles are cyclically loaded at the boundary with a lithium concentration increment  $\Delta c = 120000$  mol/m<sup>3</sup> to  $c_{max} = 480000$  mol/m<sup>3</sup> and unloaded again to the initial concentration. Accordingly, we have used approximately 248 726  $H_1$  elements for this setup. Since, here the rate-dependent problem is considered, for the time increment of the cyclic charge/discharge process, we set  $\Delta t = 500$  s.

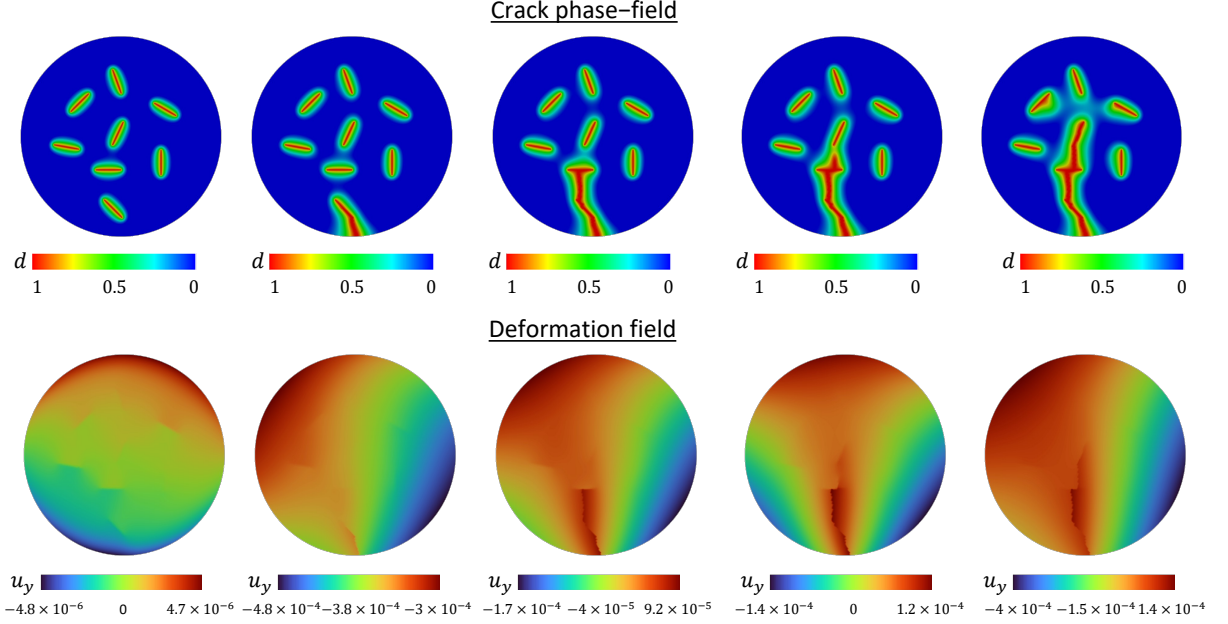


**Figure 18:** Example 3 (monotonic lithiation). Development of the crack phase-field in electrode particles and different deformation stages up to complete failure.

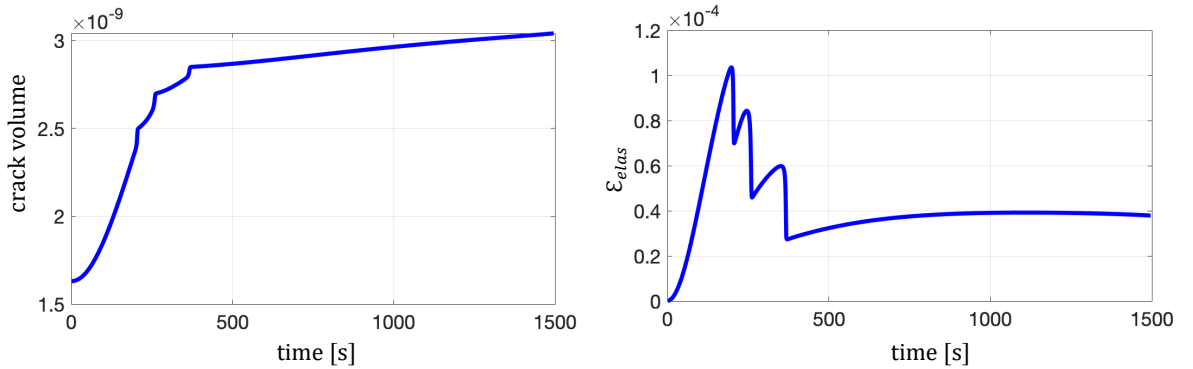


**Figure 19:** Example 3 (monotonic lithiation). Evaluation of the fracture volumes and bulk energy functional for an arbitrary Gaussian integration point for electrode particles.

Our goal here is to confirm the good performance of the proposed formulation toward a three-dimensional setting. Specifically, the influence of the micro cavities in the real three-dimensional electrode particle toward the lifespan of the lithium ion battery was briefly reported. The evolution of the crack phase-field  $d$  up to complete failure is provided in Figure 24 at nine deformation stages up to final failure. The crack initiates at the tip of different pre-defined micro cavities and continues to propagate toward merging. The crack branching at different stages also observed, in which the complex three-dimensional crack structure isosurface with  $\{\hat{d} := 1 \text{ if } d \geq 0.99 \text{ otherwise } \hat{d} := 0\}$ , see Figure 24.

Considering the multiphysics setting of the problem, the computational CPU time is prohibitive. By using MPI with the FEniCS open platform, we can distribute the computational load for fatigue failure analysis. This allows us to resolve the resulting crack path with higher resolution by utilizing multiple cores in our analysis. Additionally, the phase-field formulation of fracture is inherently nonlinear, demanding the resolution of

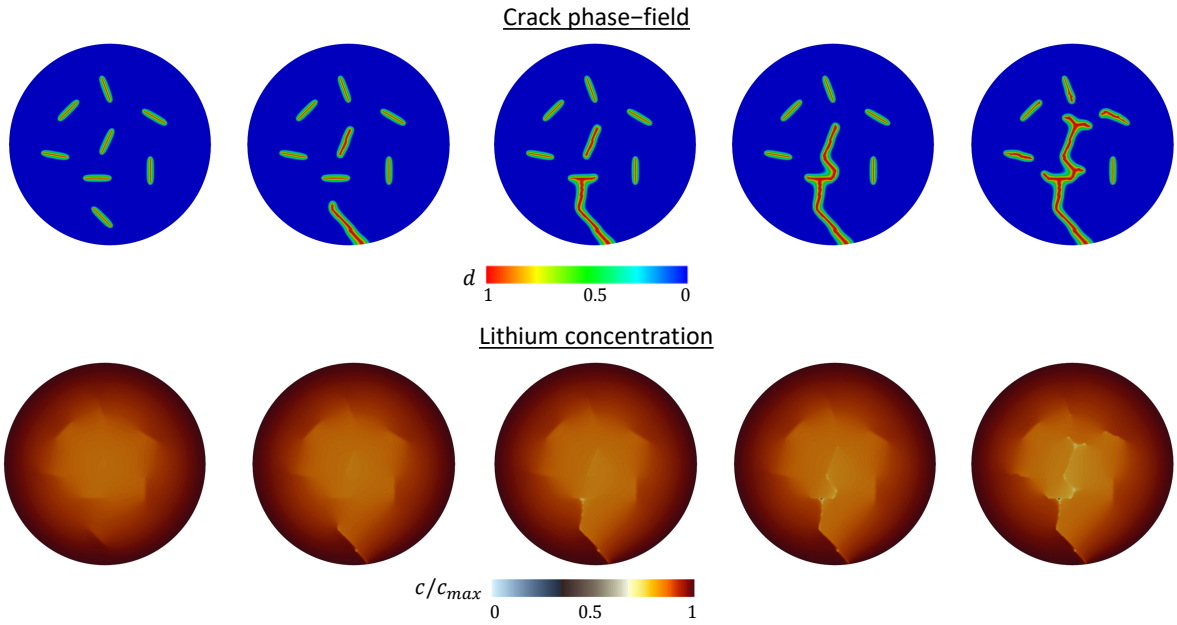


**Figure 20:** Example 3 (cyclic lithiation/delithiation). Development of the crack phase-field in electrode particles and different lithium concentration up to complete failure.

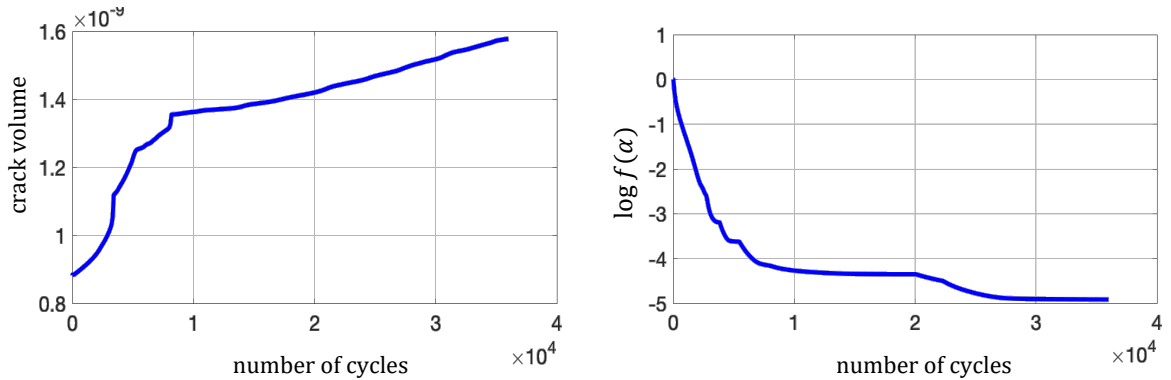


**Figure 21:** Example 3 (cyclic lithiation/delithiation). Evaluation of the fracture volumes and fatigue degradation functions for an arbitrary Gaussian integration point for electrode particles.

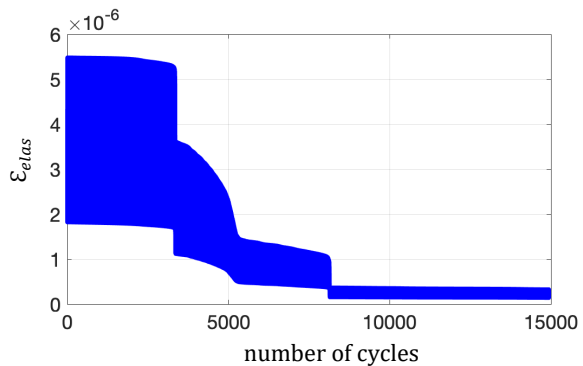


**Figure 22:** Example 3. The accumulated elastic energy functional with respect to the number of cycles.

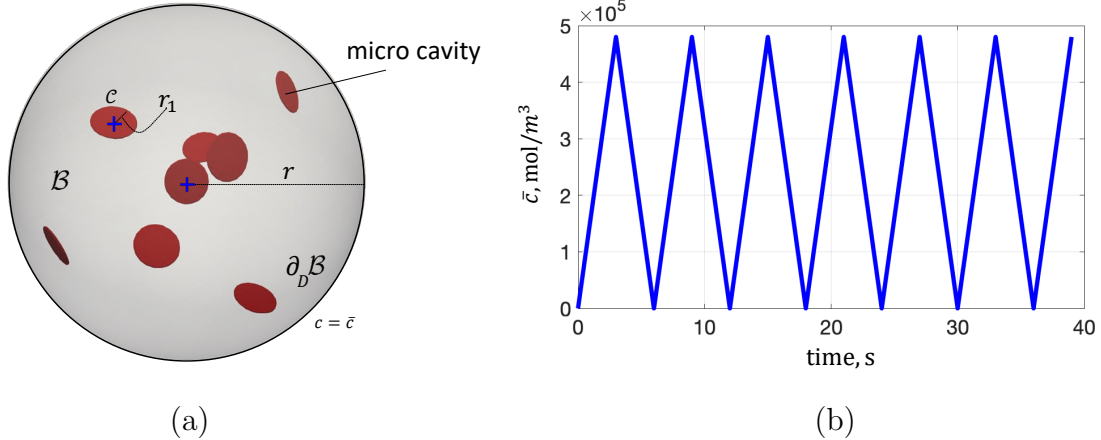


**Figure 23:** Example 4. The representation of the spherical electrode particle with 8 randomly distributed micro cavities. (a) Geometry and boundary conditions, and (b) cyclic lithiation/delithiation concentration load.

small-length scales. Consequently, along with our simulation, parallel computing becomes a crucial necessity for addressing such complex multiphysics problems, specifically for fatigue cracking. This is mainly because fatigue cracking requires many cycles of lithiation and delithiation to have a complete failure of electrode particles. Thus, to evaluate parallel computation, we focus on the fatigue degradation mechanisms of electrode particles using the boundary value problem (BVP) illustrated in Figure 23. Therefore the efficiency of parallel computing, we employ a multiple cores sub-regional computing approach, as depicted in Figure 25. We have observed, that increasing the number of CPUs serves to distribute the workload among cores, leading to improved computational efficiency.

We further investigated the model's wall time for varying CPU counts (as shown in Figure 26), where we tested configurations with 4 to 64 CPUs. As expected, increasing the number of CPUs reduces the workload on each individual core, leading to improved efficiency. The results demonstrate that efficient parallel computation and a well-defined solver can achieve significant time savings in CPU usage.

In summary, the presence of cracks applies an important impact on the integrity and structure of the electrode particle, compromising its functionality and overall performance. These cracks contribute to the degradation and destabilization of the electrode, potentially impeding its efficiency in various applications. Thus, providing a mathematical framework as well as modeling of lithium diffusion-induced fatigue cracking is crucial for the prediction of the lifetime balance of lithium-ion battery.

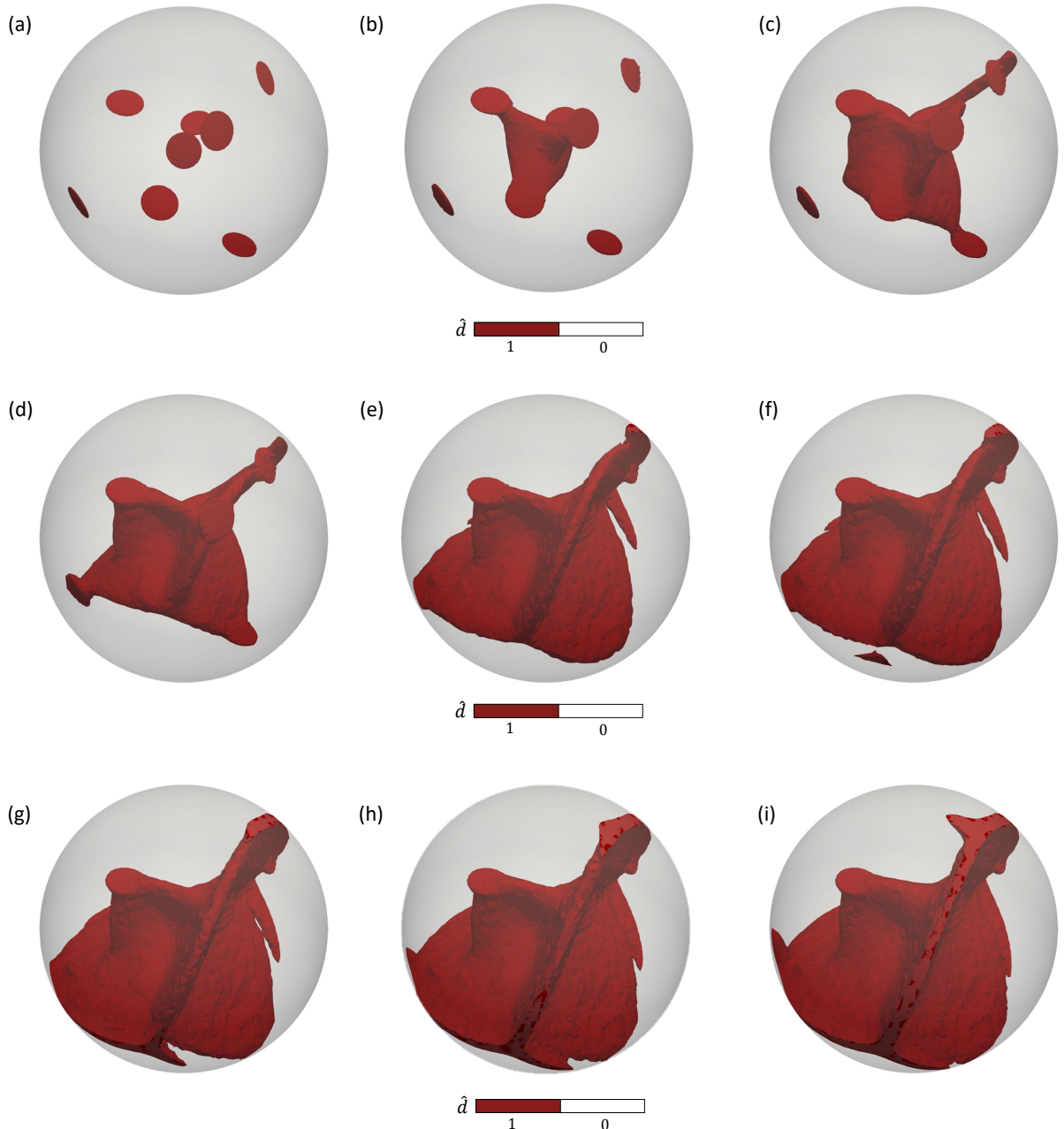


**Figure 24:** Example 4. Evaluation of the fracture pattern with crack isosurface evolution with  $\{\hat{d} := 1 \text{ if } d \geq 0.99 \text{ otherwise } \hat{d} := 0\}$ , normalized lithium concentration for nine radial deformations from (a) nucleation, (b)-(h) fracture propagation, and (i) stabilization of the crack.

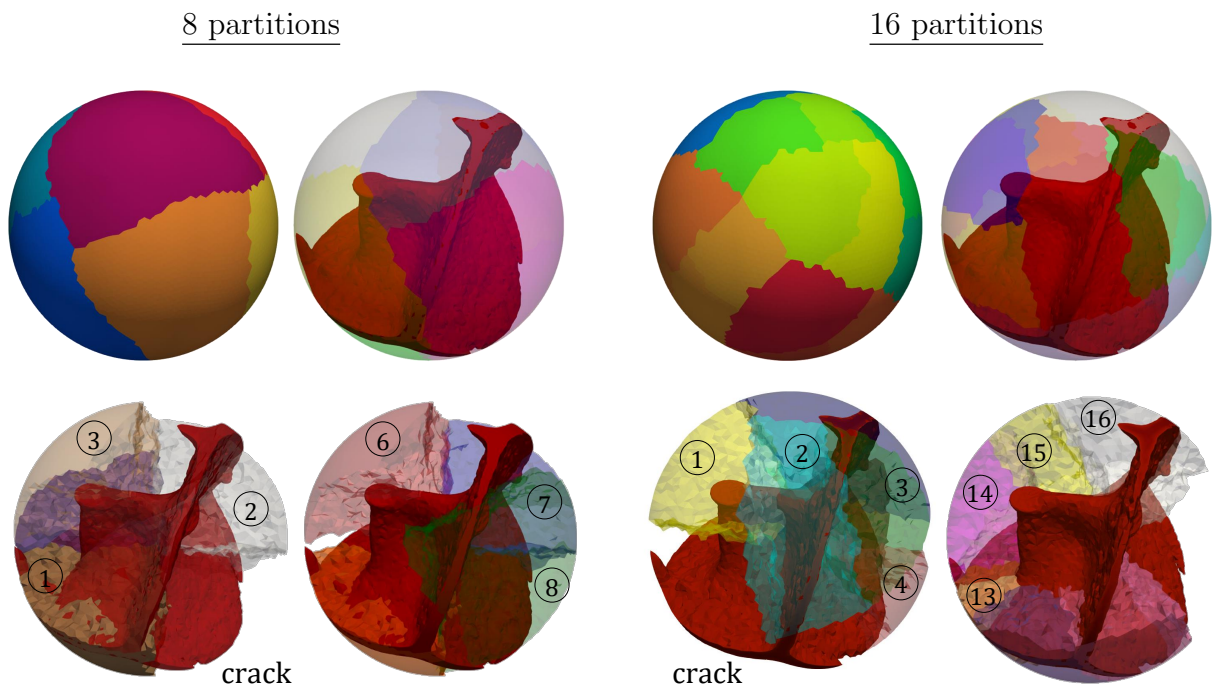


**Figure 25:** Example 4. The representation of the three-dimensional electrode particle in the lithium ion battery of the meshes partitioned for 8 cores (left side), and 16 cores (right side) for the complete failure.

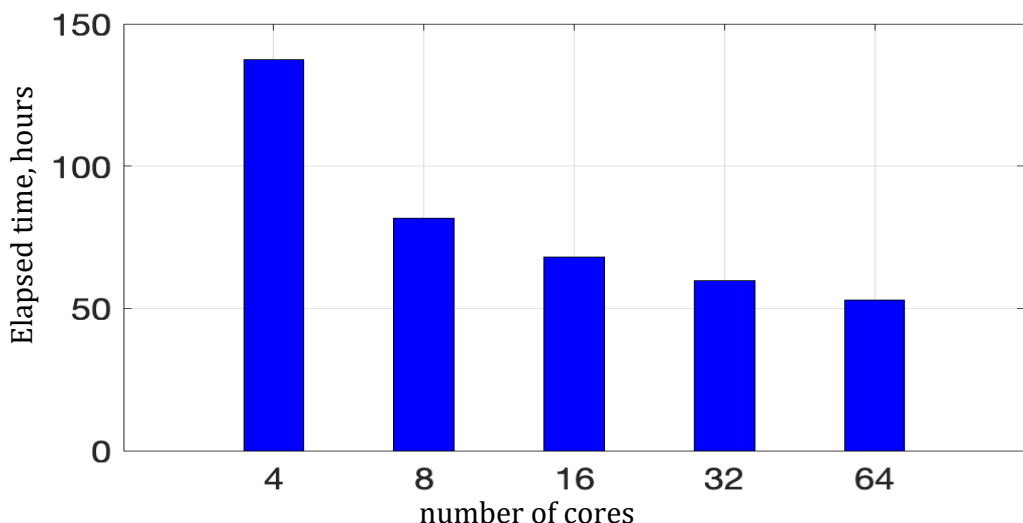


**Figure 26:** Example 4. Performance of parallel computing for different numbers of CPUs (cores) applied to the three-dimensional setting due to cyclic loading. The elapsed CPU time is shown for different hours.



## 4. Conclusion

This study outlined a robust and efficient mathematical formulation for both monotonic and fatigue failure theory in lithium-ion battery electrode particles for lithium diffusion induced fracture. The developed chemo-mechanical model undergoes fatigue failure package is written in FEniCS as a popular free open-source computing platform for solving partial differential equations in which simplifies the implementation of parallel FEM simulations. We can estimate the degradation mechanism of the electrode particles and, thus, help *to enhance the fracture resistance of lithium-ion batteries*. Thus, our detailed multiphysics modeling and implementation within an open-source code can be used further to develop additional constitutive law to capture different degradation mechanics within lithium ion batteries.

Four numerical examples with different boundary value problems including various test cases were presented to substantiate our algorithmic developments. Both monotonic charge process and fatigue charge/discharge process are presented in both theoretical and implementation point of view. Through these numerical examples, our primary objective was to examine the impact of the random distribution of micro cavities (voids) and micro notches on the fracture resistance within the electrode particle during the processes of lithiation/delithiation. It has been observed that the size and volume of micro pores and micro cavities (pre-defined notches) have a great influence on resulting crack pattern. The presence of these cracks is observed to have a significant adverse effect on the integrity and structure of the electrode particle, compromising its functionality and overall performance. These cracks contribute to the degradation and destabilization of the electrode, potentially impeding its efficiency in various applications. Thus our findings demonstrate that the concentration of lithium experiences a notable increase near the tip of a crack within an electrode particle. This phenomenon is primarily attributed to the intense hydrostatic stresses in that particular region, driving the diffusion of lithium towards the crack tip. Consequently, all examined numerical studies show here, the lithium concentration peaks in the vicinity of the crack zone. In summary, the suggested formulation has the potential to enhance our understanding of the fracture mechanics in lithium-ion battery electrodes, providing valuable insights for the design of future generations of electrode structures.

## Acknowledgment

A. Khodadadian acknowledges the support by FWF (Austrian Science Fund) in the Standalone Project No P-36520, entitled Using Single Atom Catalysts as Nanozymes in FET Sensors. The authors also acknowledge Professor Nikolaos Bouklas from Cornell University for a fruitful discussion.

## Appendix A. Overview software package in FEniCS

FEniCS is an free open-source computing platform [102] for solving partial differential equations (PDEs). In fact, FEniCS helps developer and scientific researcher to rewrite a serial code into a parallel running code. The FEniCS docker container already includes MPICH and is fundamentally developed for parallel processing on laptops, workstations and also HPC clusters. The user can define the PDEs in Python that FEniCS translates

via ffc into a low-level C code, enabling the compilation of highly efficient simulations. A wide variety of elements are supported and meshes from for example GMSH can be implemented and handled very easily. FEniCS makes it easy to change and adapt the code quickly, since for example solver algorithms can be changed with simple commands and parameters. The implementation of a particular algorithm is avoided. So, a flowchart of the overall framework for the multi-field chemo-mechanical procedure for the fracture mechanism in lithium-ion battery is provided in Figure 27.

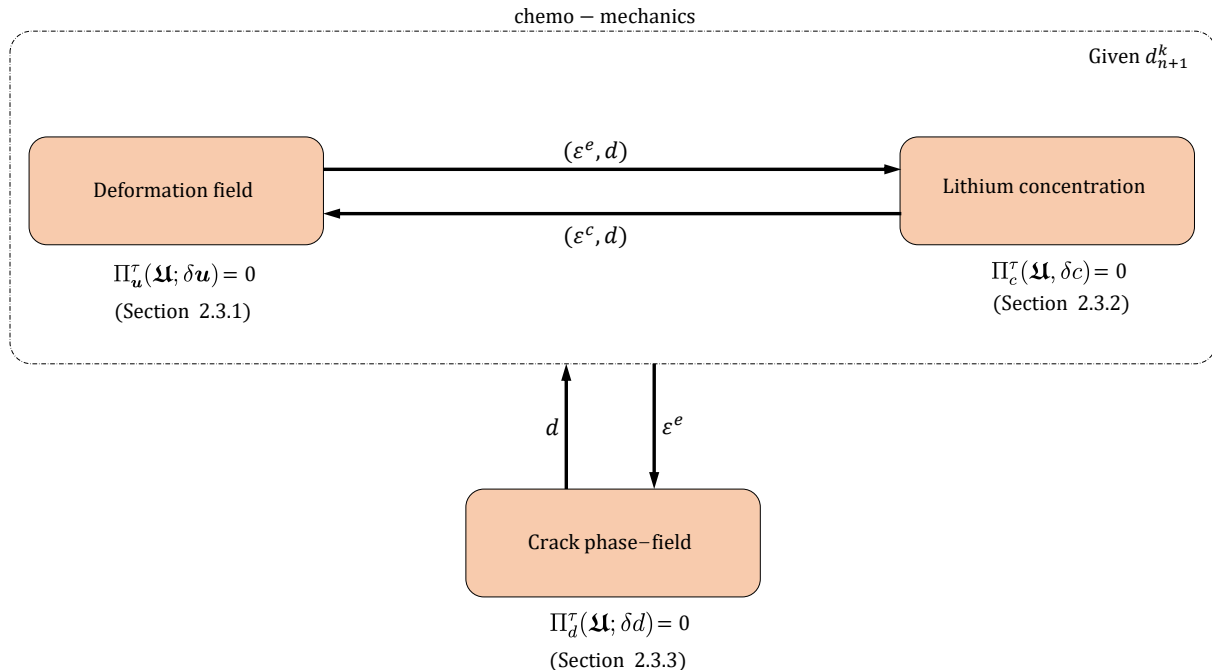


**Figure 27:** Multi-field chemo-mechanical procedure for the fracture mechanism in lithium-ion battery.

In order to summarize the code concisely, only the most important parts of the code are presented here. The library provided by FEniCS is called Dolfin. These and others must first be imported so that the required classes and tools are available for programming. The ufl library contains operators and expressions that can be used to express variational forms and functionals und PETSc (Portable, Extensible Toolkit for Scientific Computation) contains classes that are used to solve the PDEs.

```

76 from __future__ import print_function
77 from fenics import *
78 import os
79 import numpy as np

```

Now the mesh has to be imported. This was previously created in GMSH and consists of triangular elements. The physical groups, i.e. the particle surface and initial cracks, were marked with labels. This simplifies reading and referring to them. In addition, the number, position and size of the subdomains, as well as the number of elements can be easily changed in GMSH without having to adapt the FEniCS code. The information of the subdomain labels are passed to `mf`. An advantage of FEniCS is that it automatically

partitions the mesh and distributes it over the allocated cores. This is done with the argument `MPI.COMM_WORLD`. Therefore, there is no need to implement an algorithm for decomposition.

```

95 mesh = Mesh()
96
97 with XDMFFile("elliptical_battery1.xdmf") as infile:
98     infile.read(mesh)
99 mvc = MeshValueCollection("size_t", mesh, 1)
100
101 with XDMFFile("elliptical_battery1_mt.xdmf") as infile:
102     infile.read(mvc, "name_to_read")
103 mf = cpp.mesh.MeshFunctionSizet(mesh, mvc)

```

Next, we define a function space, which we use for example to define variables in which we store the solutions or to describe dirichlet boundary condition. `CG` stands for Lagrange elements and the order of the polynomials here is first-order approximation.

```

184 # for concentration: c(x,t)
185 V_c = FunctionSpace(mesh, 'CG', 1)

```

In the following, few material parameters are introduced (for exact description of material parameters see the code provided).

```

214 # phasefield properties
215 Gc = 1
216 lc = 2.*mesh.hmax()
217 kappa_d = 1e-8
218
219 # elastic properties
220 E=9.3e+4
221 nu=0.3

```

In order to implement the mathematical framework, it is sufficient to define functions as follows:

```

260 # total strain tensor
261 def epsilon(u_):
262     return sym(grad(u_))
263
264 # lithium ion strain tensor
265 def epsilon_Battery(c_):
266     return (Om_B/3)*(c_-c0)*Identity(2)
267
268 # elastic strain tensor
269 def epsilon_elastic(u_, c_):
270     return epsilon(u_) - epsilon_Battery(c_)
271
272 # effective stress tensor
273 def sigma_eff(u_, c_):
274     return 2.0*mu*epsilon_elastic(u_, c_) + lmbda*tr(
275         epsilon_elastic(u_, c_))*Identity(2)

```

```

275
276 # hydrostatic part of effective stress tensor
277 def sigma_eff_p(u_, c_):
278     return tr(sigma_eff(u_, c_))/3
279
280 # degraded stress tensor
281 def sigma(u_, d_, c_):
282     return g(d_)*sigma_eff(u_, c_)

```

- **Monotonic charge process.** The following implementation code shows how the crack driving state function  $\tilde{D}$  based on (37) is implemented for the phase-field problem in the case of the *monothonic charge process*. In this case it is a volumetric/deviatoric split of the elastic energy density.

```

299 # effective elastic energy
300 def psip_eff(u_, c_):
301     tre=tr(epsilon_elastic(u_, c_))
302     dev_et=dev(epsilon_elastic(u_, c_))
303     return (0.5*kappa*(Pls(tre))**2+mu*inner(dev_et,dev_et))
304
305 # crack driving force
306 def psip(u_, c_):
307     return (2*l_c/G_f)*psip_eff(u_, c_)

```

The history field  $\mathcal{H}$  according to (36) is implemented with the help of a `conditional` and the keyword `lt`, which stands for *lower than*. This means that the function `H(u_, c_)` returns the value `psip(u_, c_)` if `H_n` is smaller than `psip(u_, c_)`. Otherwise the value `H_n` is returned.

```

324 def H(u_,c_):
325     return conditional(lt(H_n, psip(u_,c_)), psip(u_,c_), H_n)

```

- **Fatigue charge/discharge process.** The following part of the code shows how the crack driving state function  $\tilde{D}$  based on (38) is implemented for the phase-field problem in the case of the *fatigue charge/discharge process*. First, we define the fatigue degradation function `falp(f_)`, which is used according to (38) to degrade the critical energy release rate `Gc`. It can be seen that the fatigue degradation function is divided into three parts. The entire function is explained here using line 281. The keyword `le` means *lower or equal*. If `f_` is less than or equal to `alp_T`, the value `1` is returned. Otherwise the value `tolf`, which is approximately `0`. In the next lines, `gt` means *greater than* and `ge` *greater or equal*.

```

312 # fatigue degradation function
313 def falp(f_):
314     tolf = 1E-15
315     af = conditional(le(f_,alp_T), 1., tolf) \
316         + conditional(gt(f_,alp_T), (1.-k_fg*LOG(f_/alp_T))**2, ...
317             tolf) \
318             + conditional(ge(f_,alp_T*10**(1/k_fg)), -(1-k_fg*LOG(f_/
319                 alp_T))**2, tolf)
320     return af

```

```

319
320 # degraded Griffith's criterion
321 Gf = Gc*falp(alph)

```

In this case the elastic energy density is split into volumetric and deviatoric parts.

```

323 # effective elastic energy
324 def psip_eff(u_, c_):
325     tre=tr(epsilon_elastic(u_, c_))
326     dev_et=dev(epsilon_elastic(u_, c_))
327     return (0.5*kappa*(Pls(tre))**2+mu*inner(dev_et,dev_et))
328
329 # crack driving force
330 def psip(u_, c_):
331     return (2*lc/Gf)*psip_eff(u_, c_)

```

The history field  $\mathcal{H}$  according to (36) is implemented again with the help of a `conditional...` and the keyword `lt`, which stands for *lower than*. This means that the function  $\mathcal{H}(u_{...}, c_{...})$  returns the value  $psip(u_{...}, c_{...})$  if  $\mathcal{H}_n$  is smaller than  $psip(u_{...}, c_{...})$ . Otherwise the value  $\mathcal{H}_n$  is returned.

```

348 def H(u_,c_):
349     return conditional(lt(H_n, psip(u_,c_)), psip(u_,c_), H_n)

```

To define the Dirichlet boundary conditions for the concentration, a so-called `Expression...` must be defined first. We assign the value 0 to this expression for now. In our case the label value 1 was assigned to the particle surface. This informations will be passed together with the function space `v_c` to the function `DirichletBC`. With progressive time steps the expression `c_D1` can be overwritten and the dirichlet boundary conditions are updated automatically. For the phase field problem, the phase field variable on initial cracks is set to the value 1.

```

346 c_D1 = Expression("t",t = 0.0, degree = 0)
347 bc_c = [DirichletBC(V_c, c_D1, mf, 1)]
348
349 bc_u = []
350
351 bc_phi = DirichletBC(V_d, Constant(1), mf, 2)

```

Following (E), (D), and (C), we write the equations to be solved as:

```

359 E_u = inner(sigma(du, d, c), epsilon(var_u))*dx

```

```

370 E_phi = (-lc**2*dot(grad(dd),grad(var_d))-dd*var_d+(1-kappa_d)*(1-...
dd)*H(u,c)*var_d)*dx

```

```

381 E_conc = (((c - c_n)/tau_c_eq)*var_c + (g(d)*DB * dot(grad(c), ...
grad(var_c)))-(c*c2)*dot(grad(g(d)*sigma_eff_p(u, c)), grad(... 
var_c)))*dx

```

We note that in code within variational equation for the lithium concentration, for sake of easiness, we set  $c_2 = D\Omega_c/R\vartheta$ . To create a solver, a few lines are necessary. Here the information, such as equation to be solved and the dirichlet boundary conditions are combined.

```

372 problem_phi = LinearVariationalProblem(lhs(E_phi), rhs(E_phi), d, ...
bc_phi)
373
374 solver_phi = LinearVariationalSolver(problem_phi)
375 solver_phi.parameters["linear_solver"] = "mumps"

```

Before the PDEs are solved, the files in which the solutions are to be saved are first created. Here we have decided to use XDMF files as they are very suitable for parallel computation.

```

399 file_p = XDMFFile("./results/phi.xdmf")
400 file_c = XDMFFile("./results/conc.xdmf")
401 file_d = XDMFFile("./results/disp.xdmf")
402 file_s = XDMFFile("./results/sigma.xdmf")

```

- **Monotonic charge process.** As this is a monotonically increasing concentration, the variable `conc` is increased by the concentration increment  $\Delta c$  in each time increment. This can be used to overwrite the value `t` in the `Expression c_D1`, which is embedded in the boundary condition for the concentration.

```

426     conc += _c
427     c_D1.t = c0 + conc

```

- **Fatigue charge/discharge process.** Starting from the initial concentration, the concentration on the surface of the battery electrodes is changed cyclically (charging/discharging). For this purpose, an algorithm was written that determines the new concentration increment, here called `conc`, of the respective time step. This can be used to overwrite the value `t` in the `Expression c_D1`, which is embedded in the boundary condition for the concentration. It is important to note that one run of the algorithm means two cycles.

```

424     t += Uincr
425     j +=1
426     tloc = t
427     ncycle = 1
428     while(tloc >= tper):
429         tloc = tloc - tper
430         ncycle+= 1
431     if (tloc < qper):
432         c_load = usgn*((u_max - u_r)*tloc/qper + u_r)

```

```

433     elif (tloc >= qper) & (tloc < 2.*qper):
434         c_load = usgn*((u_r-u_max)/qper*(tloc-qper) + u_max)
435     elif (tloc >= 2.*qper) & (tloc < 3.*qper):
436         c_load = usgn*((u_min-u_r)/qper*(tloc-2.*qper) + u_r)
437     elif (tloc >= 3.*qper) & (tloc < tper):
438         c_load = usgn*((u_r-u_min)/qper*(tloc-3.*qper) + u_min)
439     c_D1.t = c0+c_load

```

To solve a variational problem, a simple command line is sufficient.

```
453     solver_phi.solve()
```

Afterwards, the history variables can be easily updated.

```

464     # lithium concentration
465     c_n.assign(c)
466
467     # history field phase field
468     H_project = project(H(u,c), WW)
469     H_n.assign(H_project)
470
471     # fatigue parameter
472     alph_n.assign(alph)
473
474     Psip_project = project(Psip(u,d,c), V_d)
475     Psip_n.assign(Psip_project)
476
477     # stress tensor
478     sig_project = project(sigma(u, d, c), TT)
479     sig.assign(sig_project)

```

The solutions of every tenth time step are then saved.

```

484     if (t % 10 == 0) or (t == n_Step):
485         file_p.write(d, t)
486         file_c.write(c, t)
487         file_d.write(u, t)
488         file_s.write(sig, t)

```

We note that by using MPI running of the FEniCS open platform, we can distribute the computational load for fatigue failure analysis in a multiphysics setting to the multiple cores by: `mpirun -np number[cores] python3 name[script].py`.

## References

- [1] D. F. Dominković, I. Bačeković, B. Čosić, G. Krajačić, T. Pukšec, N. Duić, and N. Markovska, “Zero carbon energy system of south east europe in 2050,” *Applied Energy*, vol. 184, pp. 1517–1528, 2016.
- [2] I. Tsiropoulos, W. Nijs, D. Tarvydas, P. Ruiz, *et al.*, “Towards net-zero emissions in the eu energy system by 2050,” *Insights from Scenarios in Line with the*, vol. 2030, 2020.
- [3] B. Diouf and R. Pode, “Potential of lithium-ion batteries in renewable energy,” *Renewable Energy*, vol. 76, pp. 375–380, 2015.
- [4] H. Gong and A. D. Andersen, “The role of material resources for rapid technology diffusion in net-zero transitions: Insights from ev lithium-ion battery technological innovation system in china,” *Technological Forecasting and Social Change*, vol. 200, p. 123141, 2024.
- [5] A. Olabi and M. A. Abdelkareem, “Renewable energy and climate change,” *Renewable and Sustainable Energy Reviews*, vol. 158, p. 112111, 2022.
- [6] S. J. Davis, N. S. Lewis, M. Shaner, S. Aggarwal, D. Arent, I. L. Azevedo, S. M. Benson, T. Bradley, J. Brouwer, Y.-M. Chiang, *et al.*, “Net-zero emissions energy systems,” *Science*, vol. 360, no. 6396, p. eaas9793, 2018.
- [7] S. Chu and A. Majumdar, “Opportunities and challenges for a sustainable energy future,” *nature*, vol. 488, no. 7411, pp. 294–303, 2012.
- [8] M. Armand, P. Axmann, D. Bresser, M. Copley, K. Edström, C. Ekberg, D. Guyomard, B. Lestriez, P. Novák, M. Petranikova, *et al.*, “Lithium-ion batteries—current state of the art and anticipated developments,” *Journal of Power Sources*, vol. 479, p. 228708, 2020.
- [9] C. P. Grey and D. S. Hall, “Prospects for lithium-ion batteries and beyond—a 2030 vision,” *Nature Communications*, vol. 11, no. 1, p. 6279, 2020.
- [10] R. Korthauer, *Lithium-ion batteries: basics and applications*. Springer, 2018.
- [11] M. Wakihara and O. Yamamoto, *Lithium ion batteries: fundamentals and performance*. John Wiley & Sons, 2008.
- [12] R. Xu and K. Zhao, “Corrosive fracture of electrodes in li-ion batteries,” *Journal of the Mechanics and Physics of Solids*, vol. 121, pp. 258–280, 2018.
- [13] M. R. Palacín and A. de Guibert, “Why do batteries fail?,” *Science*, vol. 351, no. 6273, p. 1253292, 2016.
- [14] N. Lin, Z. Jia, Z. Wang, H. Zhao, G. Ai, X. Song, Y. Bai, V. Battaglia, C. Sun, J. Qiao, *et al.*, “Understanding the crack formation of graphite particles in cycled commercial lithium-ion batteries by focused ion beam-scanning electron microscopy,” *Journal of power sources*, vol. 365, pp. 235–239, 2017.
- [15] H. Zheng, L. Zhang, G. Liu, X. Song, and V. S. Battaglia, “Correlationship between electrode mechanics and long-term cycling performance for graphite anode in lithium ion cells,” *Journal of Power Sources*, vol. 217, pp. 530–537, 2012.
- [16] S. Müller, P. Pietsch, B.-E. Brandt, P. Baade, V. De Andrade, F. De Carlo, and V. Wood, “Quantification and modeling of mechanical degradation in lithium-ion batteries based on nanoscale imaging,” *Nature Communications*, vol. 9, no. 1, p. 2340, 2018.

- [17] M. Makki, G. Ayoub, C. W. Lee, C. Bae, and X. Colin, “Effect of battery fast cyclic charging on the mechanical and fracture behavior of the lithium-ion battery separator,” *Polymer Degradation and Stability*, vol. 216, p. 110469, 2023.
- [18] W. Ai, B. Wu, and E. Martínez-Pañeda, “A coupled phase field formulation for modelling fatigue cracking in lithium-ion battery electrode particles,” *Journal of Power Sources*, vol. 544, p. 231805, 2022.
- [19] I. Laresgoiti, S. Käbitz, M. Ecker, and D. U. Sauer, “Modeling mechanical degradation in lithium ion batteries during cycling: Solid electrolyte interphase fracture,” *Journal of Power Sources*, vol. 300, pp. 112–122, 2015.
- [20] D. Inc., “Duracell CR-123 2/3A 3V Photo Lithium Batteries DL123.” <https://www.duracell.com/>.
- [21] T. Bernthaler, A. Kopp, A. Nagel, J. Niedermeier, G. Schneider, and F. Trier, “Microscopy analysis for green energy solutions,” *Microscopy*, 2022.
- [22] D.-S. Ko, J.-H. Park, S. Park, Y. N. Ham, S. J. Ahn, J.-H. Park, H. N. Han, E. Lee, W. S. Jeon, and C. Jung, “Microstructural visualization of compositional changes induced by transition metal dissolution in ni-rich layered cathode materials by high-resolution particle analysis,” *Nano Energy*, vol. 56, pp. 434–442, 2019.
- [23] V. Agubra and J. Fergus, “Lithium ion battery anode aging mechanisms,” *Materials*, vol. 6, no. 4, pp. 1310–1325, 2013.
- [24] I. Ryu, J. W. Choi, Y. Cui, and W. D. Nix, “Size-dependent fracture of si nanowire battery anodes,” *Journal of the Mechanics and Physics of Solids*, vol. 59, no. 9, pp. 1717–1730, 2011.
- [25] X. Zhu, Y. Chen, H. Chen, and W. Luan, “The diffusion induced stress and cracking behaviour of primary particle for li-ion battery electrode,” *International Journal of Mechanical Sciences*, vol. 178, p. 105608, 2020.
- [26] B. Bourdin, G. A. Francfort, and J.-J. Marigo, “The variational approach to fracture,” *Journal of elasticity*, vol. 91, no. 1, pp. 5–148, 2008.
- [27] P. Diehl, R. Lipton, T. Wick, and M. Tyagi, “A comparative review of peridynamics and phase-field models for engineering fracture mechanics,” *Computational Mechanics*, vol. 69, no. 6, pp. 1259–1293, 2022.
- [28] T. Wick, *Multiphysics phase-field fracture: modeling, adaptive discretizations, and solvers*, vol. 28. Walter de Gruyter GmbH & Co KG, 2020.
- [29] J.-Y. Wu, V. P. Nguyen, C. Thanh Nguyen, D. Sutula, S. Bordas, and S. Sinaie, “Phase field modelling of fracture,” *Advances in Applied Mechanics*, vol. 53, pp. 1–183, 09 2019.
- [30] B. Bourdin, G. Francfort, and J.-J. Marigo, “The variational approach to fracture,” *Journal of Elasticity*, vol. 91, pp. 5–148, 2008.
- [31] M. Ambati, T. Gerasimov, and L. De Lorenzis, “A review on phase-field models of brittle fracture and a new fast hybrid formulation,” *Computational Mechanics*, vol. 55, no. 2, pp. 383–405, 2015.
- [32] G. Francfort and J.-J. Marigo, “Revisiting brittle fracture as an energy minimization problem,” *Journal of the Mechanics and Physics of Solids*, vol. 46, no. 8, pp. 1319–1342, 1998.
- [33] B. Bourdin, G. Francfort, and J.-J. Marigo, “Numerical experiments in revisited brittle fracture,” *Journal of the Mechanics and Physics of Solids*, vol. 48, no. 4, pp. 797–826, 2000.

- [34] B. Bourdin, J.-J. Marigo, C. Maurini, and P. Sicsic, “Morphogenesis and propagation of complex cracks induced by thermal shocks,” *Physical review letters*, vol. 112, no. 1, p. 014301, 2014.
- [35] C. Miehe, L.-M. Schaenzel, and H. Ulmer, “Phase field modeling of fracture in multi-physics problems. part i. balance of crack surface and failure criteria for brittle crack propagation in thermo-elastic solids,” *Computer Methods in Applied Mechanics and Engineering*, vol. 294, pp. 449–485, 2015.
- [36] C. Miehe, M. Hofacker, L.-M. Schänzel, and F. Aldakheel, “Phase field modeling of fracture in multi-physics problems. part ii. coupled brittle-to-ductile failure criteria and crack propagation in thermo-elastic-plastic solids,” *Computer Methods in Applied Mechanics and Engineering*, vol. 294, pp. 486–522, 2015.
- [37] F. Aldakheel, N. Noii, T. Wick, and P. Wriggers, “A global-local approach for hydraulic phase-field fracture in poroelastic media,” *Computers and Mathematics with Applications*, 2020.
- [38] M. Abubakar Ali, C. Tomann, F. Aldakheel, M. Mahlbacher, N. Noii, N. Oneschkow, K.-H. Drake, L. Lohaus, P. Wriggers, and M. Haist, “Influence of moisture content and wet environment on the fatigue behaviour of high-strength concrete,” *Materials*, vol. 15, no. 3, p. 1025, 2022.
- [39] J. Ulloa, N. Noii, R. Alessi, F. Aldakheel, G. Degrande, and S. François, “Variational modeling of hydromechanical fracture in saturated porous media: A micromechanics-based phase-field approach,” *Computer Methods in Applied Mechanics and Engineering*, vol. 396, p. 115084, 2022.
- [40] N. Noii, A. Khodadadian, J. Ulloa, F. Aldakheel, T. Wick, S. François, and P. Wriggers, “Bayesian inversion for unified ductile phase-field fracture,” *Computational Mechanics*, vol. 68, no. 4, pp. 943–980, 2021.
- [41] T. Wick, “Goal functional evaluations for phase-field fracture using pu-based dwr mesh adaptivity,” *Computational Mechanics*, vol. 57, no. 6, pp. 1017–1035, 2016.
- [42] S. Lee, A. Mikelić, M. F. Wheeler, and T. Wick, “Phase-field modeling of proppant-filled fractures in a poroelastic medium,” *Computer Methods in Applied Mechanics and Engineering*, vol. 312, pp. 509–541, 2016.
- [43] A. Mikelić, M. F. Wheeler, and T. Wick, “A phase-field method for propagating fluid-filled fractures coupled to a surrounding porous medium,” *Multiscale Modeling & Simulation*, vol. 13, no. 1, pp. 367–398, 2015.
- [44] S. Lee, M. F. Wheeler, and T. Wick, “Pressure and fluid-driven fracture propagation in porous media using an adaptive finite element phase field model,” *Computer Methods in Applied Mechanics and Engineering*, vol. 305, pp. 111–132, 2016.
- [45] C. Miehe, S. Mauthe, and S. Teichtmeister, “Minimization principles for the coupled problem of darcy-biot-type fluid transport in porous media linked to phase field modeling of fracture,” *Journal of the Mechanics and Physics of Solids*, vol. 82, pp. 186–217, 2015.
- [46] C. Miehe and S. Mauthe, “Phase field modeling of fracture in multi-physics problems. part iii. crack driving forces in hydro-poro-elasticity and hydraulic fracturing of fluid-saturated porous media,” *Computer Methods in Applied Mechanics and Engineering*, vol. 304, pp. 619–655, 2016.
- [47] B. Markert and Y. Heider, “Coupled multi-field continuum methods for porous media fracture,” in *Recent Trends in Computational Engineering - CE2014* (M. Mehl, M. Bischoff, and M. Schäfer, eds.), vol. 105 of *Lecture Notes in Computational Science and Engineering*, pp. 167–180, Cham and Heidelberg and New York and Dordrecht and London: Springer, 2015.

- [48] Y. Heider and B. Markert, “A phase-field modeling approach of hydraulic fracture in saturated porous media,” *Mechanics Research Communications*, vol. 80, pp. 38–46, 2017.
- [49] Z. A. Wilson and C. M. Landis, “Phase-field modeling of hydraulic fracture,” *Journal of the Mechanics and Physics of Solids*, vol. 96, pp. 264–290, 2016.
- [50] M. J. Borden, C. V. Verhoosel, M. A. Scott, T. J. Hughes, and C. M. Landis, “A phase-field description of dynamic brittle fracture,” *Computer Methods in Applied Mechanics and Engineering*, vol. 217-220, pp. 77–95, 2012.
- [51] E. Tanné, T. Li, B. Bourdin, J.-J. Marigo, and C. Maurini, “Crack nucleation in variational phase-field models of brittle fracture,” *Journal of the Mechanics and Physics of Solids*, vol. 110, pp. 80–99, 2018.
- [52] A. Schlüter, A. Willenbücher, C. Kuhn, and R. Müller, “Phase field approximation of dynamic brittle fracture,” *Computational Mechanics*, vol. 54, no. 5, pp. 1141–1161, 2014.
- [53] J. Carlsson and P. Isaksson, “Dynamic crack propagation in wood fibre composites analysed by high speed photography and a dynamic phase field model,” *International Journal of Solids and Structures*, vol. 144-145, pp. 78–85, 2018.
- [54] C. Miehe, F. Welschinger, and F. Aldakheel, “Variational gradient plasticity at finite strains. part ii: Local-global updates and mixed finite elements for additive plasticity in the logarithmic strain space,” *Computer Methods in Applied Mechanics and Engineering*, vol. 268, pp. 704–734, 2014.
- [55] M. Ambati and L. de Lorenzis, “Phase-field modeling of brittle and ductile fracture in shells with isogeometric nurbs-based solid-shell elements,” *Computer Methods in Applied Mechanics and Engineering*, vol. 312, pp. 351–373, 2016.
- [56] M. J. Borden, T. J. Hughes, C. M. Landis, A. Anvari, and I. J. Lee, “A phase-field formulation for fracture in ductile materials: Finite deformation balance law derivation, plastic degradation, and stress triaxiality effects,” *Computer Methods in Applied Mechanics and Engineering*, vol. 312, pp. 130–166, 2016.
- [57] P. Shanthraj, L. Sharma, B. Svendsen, F. Roters, and D. Raabe, “A phase field model for damage in elasto-viscoplastic materials,” *Computer Methods in Applied Mechanics and Engineering*, vol. 312, pp. 167–185, 2016.
- [58] V. P. Nguyen and J.-Y. Wu, “Modeling dynamic fracture of solids with a phase-field regularized cohesive zone model,” *Computer Methods in Applied Mechanics and Engineering*, vol. 340, pp. 1000–1022, 2018.
- [59] C. V. Verhoosel and R. de Borst, “A phase-field model for cohesive fracture,” *International Journal for Numerical Methods in Engineering*, vol. 96, no. 1, pp. 43–62, 2013.
- [60] J. Vignollet, S. May, R. de Borst, and C. V. Verhoosel, “Phase-field models for brittle and cohesive fracture,” *Meccanica*, vol. 49, no. 11, pp. 2587–2601, 2014.
- [61] Hirshikesh, S. Natarajan, and R. K. Annabattula, “Modeling crack propagation in variable stiffness composite laminates using the phase field method,” *Composite Structures*, vol. 209, pp. 424–433, 2019.
- [62] Hirshikesh, S. Natarajan, R. K. Annabattula, and E. Martínez-Pañeda, “Phase field modelling of crack propagation in functionally graded materials,” *Composites Part B: Engineering*, vol. 169, pp. 239–248, 2019.

- [63] N. Noii, H. A. Jahangiry, and H. Waisman, “Level-set topology optimization for ductile and brittle fracture resistance using the phase-field method,” *Computer Methods in Applied Mechanics and Engineering*, vol. 409, p. 115963, 2023.
- [64] J. B. Russ and H. Waisman, “A novel elastoplastic topology optimization formulation for enhanced failure resistance via local ductile failure constraints and linear buckling analysis,” *Computer Methods in Applied Mechanics and Engineering*, vol. 373, p. 113478, 2021.
- [65] L. Xia, D. Da, and J. Yvonnet, “Topology optimization for maximizing the fracture resistance of quasi-brittle composites,” *Computer Methods in Applied Mechanics and Engineering*, vol. 332, pp. 234–254, 2018.
- [66] N. Noii, A. Khodadadian, J. Ulloa, F. Aldakheel, T. Wick, S. François, and P. Wriggers, “Bayesian inversion with open-source codes for various one-dimensional model problems in computational mechanics,” *Archives of Computational Methods in Engineering*, pp. 1–34, 2022.
- [67] N. Noii, A. Khodadadian, and F. Aldakheel, “Probabilistic failure mechanisms via monte carlo simulations of complex microstructures,” *Computer Methods in Applied Mechanics and Engineering*, vol. 399, p. 115358, 2022.
- [68] R. J. LeVeque, “Top ten reasons to not share your code (and why you should anyway),” *SIAM News*, vol. 46, no. 3, 2013.
- [69] H. Anzt, F. Bach, S. Druskat, F. Löffler, A. Loewe, B. Y. Renard, G. Seemann, A. Struck, E. Achhammer, P. Aggarwal, *et al.*, “An environment for sustainable research software in germany and beyond: current state, open challenges, and call for action,” *F1000Research*, vol. 9, 2020.
- [70] P. Farrell and C. Maurini, “Linear and nonlinear solvers for variational phase-field models of brittle fracture,” *International Journal for Numerical Methods in Engineering*, vol. 109, no. 5, pp. 648–667, 2017.
- [71] R. G. Tangella, P. Kumbhar, and R. K. Annabattula, “Hybrid phase-field modeling of thermo-elastic crack propagation,” *International Journal for Computational Methods in Engineering Science and Mechanics*, vol. 23, no. 1, pp. 29–44, 2022.
- [72] S. Natarajan, R. K. Annabattula, E. Martínez-Pañeda, *et al.*, “Phase field modelling of crack propagation in functionally graded materials,” *Composites Part B: Engineering*, vol. 169, pp. 239–248, 2019.
- [73] K. Seleš, T. Lesičar, Z. Tonković, and J. Sorić, “A residual control staggered solution scheme for the phase-field modeling of brittle fracture,” *Engineering Fracture Mechanics*, vol. 205, pp. 370–386, 2019.
- [74] Hirshikesh, S. Natarajan, and R. K. Annabattula, “A fenics implementation of the phase field method for quasi-static brittle fracture,” *Frontiers of Structural and Civil Engineering*, vol. 13, pp. 380–396, 2019.
- [75] D. Schneider, B. Nestler, *et al.*, “Realization of adaptive mesh refinement for phase-field model of thermal fracture within the fenics framework,” *Engineering Fracture Mechanics*, vol. 293, p. 109676, 2023.
- [76] P. K. Kristensen and E. Martínez-Pañeda, “Phase field fracture modelling using quasi-newton methods and a new adaptive step scheme,” *Theoretical and Applied Fracture Mechanics*, vol. 107, p. 102446, 2020.
- [77] Y. Navidtehrani, C. Betegón, and E. Martínez-Pañeda, “A simple and robust abaqus implementation of the phase field fracture method,” *Applications in Engineering Science*, vol. 6, p. 100050, 2021.

- [78] T. Heister and T. Wick, “pfm-cracks: A parallel-adaptive framework for phase-field fracture propagation,” *Software Impacts*, vol. 6, p. 100045, 2020.
- [79] E. Korec, M. Jirásek, H. S. Wong, and E. Martínez-Pañeda, “A phase-field chemo-mechanical model for corrosion-induced cracking in reinforced concrete,” *Construction and Building Materials*, vol. 393, p. 131964, 2023.
- [80] Z. Khalil, A. Y. Elghazouli, and E. Martinez-Paneda, “A generalised phase field model for fatigue crack growth in elastic-plastic solids with an efficient monolithic solver,” *Computer Methods in Applied Mechanics and Engineering*, vol. 388, p. 114286, 2022.
- [81] V. Prakash, A. K. Behera, and M. M. Rahaman, “A phase-field model for thermo-mechanical fracture with an open-source implementation of it using gridap in julia,” *arXiv preprint arXiv:2110.12284*, 2021.
- [82] A. Khodadadian, N. Noii, M. Parvizi, M. Abbaszadeh, T. Wick, and C. Heitzinger, “A bayesian estimation method for variational phase-field fracture problems,” *Computational Mechanics*, vol. 66, no. 4, pp. 827–849, 2020.
- [83] A. Khodadadian, N. Noii, M. Parvizi, M. Abbaszadeh, T. Wick, and C. Heitzinger, “A Bayesian estimation method for variational phase-field fracture problems,” *Computational Mechanics*, vol. 66, pp. 827–849, 2020.
- [84] J. Ågren, “The onsager reciprocity relations revisited,” *Journal of Phase Equilibria and Diffusion*, vol. 43, no. 6, pp. 640–647, 2022.
- [85] C. V. Di Leo and L. Anand, “Hydrogen in metals: a coupled theory for species diffusion and large elastic-plastic deformations,” *International Journal of Plasticity*, vol. 43, pp. 42–69, 2013.
- [86] E. Martínez-Pañeda, A. Golahmar, and C. F. Niordson, “A phase field formulation for hydrogen assisted cracking,” *Computer Methods in Applied Mechanics and Engineering*, vol. 342, pp. 742–761, 2018.
- [87] P. Sofronis and R. M. McMeeking, “Numerical analysis of hydrogen transport near a blunting crack tip,” *Journal of the Mechanics and Physics of Solids*, vol. 37, no. 3, pp. 317–350, 1989.
- [88] F. Aldakheel, *Mechanics of Nonlocal Dissipative Solids: Gradient Plasticity and Phase Field Modeling of Ductile Fracture*. PhD thesis, Institute of Applied Mechanics (CE), Chair I, University of Stuttgart, 2016. <http://dx.doi.org/10.18419/opus-8803>.
- [89] N. Noii, M. Fan, T. Wick, and Y. Jin, “A quasi-monolithic phase-field description for orthotropic anisotropic fracture with adaptive mesh refinement and primal-dual active set method,” *Engineering Fracture Mechanics*, vol. 258, p. 108060, 2021.
- [90] N. Noii, F. Aldakheel, T. Wick, and P. Wriggers, “An adaptive global-local approach for phase-field modeling of anisotropic brittle fracture,” *Computer Methods in Applied Mechanics and Engineering*, vol. 361, p. 112744, 2020.
- [91] C. Kuhn, A. Schlüter, and R. Müller, “On degradation functions in phase field fracture models,” *Computational Materials Science*, vol. 108, pp. 374–384, 2015.
- [92] J.-Y. Wu, “A unified phase-field theory for the mechanics of damage and quasi-brittle failure,” *Journal of the Mechanics and Physics of Solids*, vol. 103, pp. 72–99, 2017.
- [93] J.-Y. Wu, V. Nguyen, C. Nguyen, D. Sutula, S. Bordas, and S. Sinaie, “Phase field modeling of fracture,” *Advances in Applied Mechanics: Multi-Scale Theory and Computation*, vol. 52, 2018.

- [94] F. Aldakheel, N. Noii, T. Wick, O. Allix, and P. Wriggers, “Multilevel global-local techniques for adaptive ductile phase-field fracture,” *Computer Methods in Applied Mechanics and Engineering*, vol. 387, p. 114175, 2021.
- [95] M. Ambati, T. Gerasimov, and L. De Lorenzis, “A review on phase-field models of brittle fracture and a new fast hybrid formulation,” *Computational Mechanics*, vol. 55, no. 2, pp. 383–405, 2015.
- [96] N. Noii and T. Wick, “A phase-field description for pressurized and non-isothermal propagating fractures,” *Computer Methods in Applied Mechanics and Engineering*, vol. 351, pp. 860 – 890, 2019.
- [97] P. Carrara, M. Ambati, R. Alessi, and L. De Lorenzis, “A framework to model the fatigue behavior of brittle materials based on a variational phase-field approach,” *Computer Methods in Applied Mechanics and Engineering*, vol. 361, p. 112731, 2020.
- [98] C. Miehe, F. Welschinger, and M. Hofacker, “Thermodynamically consistent phase-field models of fracture: Variational principles and multi-field fe implementations,” *International Journal for Numerical Methods in Engineering*, vol. 83, pp. 1273–1311, 2010.
- [99] T. Gerasimov, N. Noii, O. Allix, and L. De Lorenzis, “A non-intrusive global/local approach applied to phase-field modeling of brittle fracture,” *Advanced modeling and simulation in engineering sciences*, vol. 5, no. 1, pp. 1–30, 2018.
- [100] J. ne Zeller, J.-P. D. M. Kuhn, J. Saak, and M. Blesel, “Performance analysis of mpi-based fenics/petsc models in pymor,” 2021.
- [101] J. M. Maljaars, C. N. Richardson, and N. Sime, “Leopard: A particle library for fenics,” *Computers & Mathematics with Applications*, vol. 81, pp. 289–315, 2021.
- [102] A. Logg, K.-A. Mardal, and G. Wells, *Automated solution of differential equations by the finite element method: The FEniCS book*, vol. 84. Springer Science & Business Media, 2012.